PROCEEDINGS, 45th Workshop on Geothermal Reservoir Engineering
Stanford University, Stanford, California, February 10-12, 2020
SGP-TR-216

Modeling Thermal-Hydrologic-Mechanical Processes for EGS Collab Thermal Circulation Tests using Embedded Discrete Fracture Model

Yu-Shu Wu[1], Xiangyu Yu[1], Shihao Wang[1], Cong Wang[1], Philip Winterfeld[1] and EGS-Collab Team[2]

[1]Colorado School of Mines, 1500 Illinois St, Golden CO 80401

xiyu@mymail.mines.edu

Keywords: Coupled Thermal-Hydrologic-Mechanical (THM) Model, Embedded Discrete Fracture Model (EDFM), Fractured Geothermal Reservoir, Thermal Circulation Test, EGS Collab

ABSTRACT

Engineered or Enhanced Geothermal Systems (EGS) are being investigated in a 10-20 meter scale at EGS Collab using multiple scientific monitoring, measurement and characterization tools. The research at EGS Collab will not only facilitate the Frontier Observatory for Research in Geothermal Energy (FORGE) project but also improve our understanding of subsurface stimulation and development of geothermal reservoirs. After stimulation of a hydraulic fracture, starting from May 2019, a thermal circulation test was conducted by injecting cold water into the hydraulic fracture. Endpoint temperatures (at the end of 2019) were measured and flow rate from multiple wells were monitored. With this data in hand, reservoir simulation or numerical modeling of fluid/heat flow should be applied to explore its correctness and applicability, and meanwhile better validate the characterization of the fracture system.

In this study, a coupled Thermal-Hydrologic-Mechanical (THM) simulator combined with Embedded Discrete Fracture Model (EDFM) is adopted to model the circulation process. Due to the uncertainty of fracture permeability, fracture geometry, boundary conditions, and fracture network, a thorough investigation of different scenarios has been performed. A simplified one-fracture model was first investigated, followed by a full-scale three fracture model. Several conditions of different fracture permeability, boundary conditions, geomechanics and activated natural fracture system were proposed and simulated. The simulations show that these factors all impact the results to some extent, and production temperature, flow rate and injection pressure can be approximately matched if appropriate parameters are input into the model. Further investigation should be performed with long term circulation data and more characterization data, in order to check the possibilities of these model conditions.

1. INTRODUCTION

Engineered or Enhanced Geothermal System (EGS) could potentially be a major source of clean energy for electricity generation, by heating up the cold fluid injected into the deep reservoir that needs to be artificially stimulated for a fracture network. However, there are still challenges faced by scientists and engineers to tackle: such as (1) effectively create fracture network by stimulation based on in-situ conditions; (2) measure and monitor fracture permeability evolution at reservoir scale; (3) effectively isolate the stimulation zone for multistage fracturing or flow path control; (4) provide sustainable energy from the developed geothermal systems (Kneafsey et al., 2019). EGS Collab project was initiated by the Department of Energy (DOE) to facilitate the other EGS project, Frontier Observatory for Research in Geothermal Energy (FORGE). In EGS Collab project, geological characterization, geophysical imaging and monitoring, stimulation, and flow tests and numerical simulation are all conducted to fully assist understanding the stimulation process, fracture initiation and propagation, fluid flow and heat transfer in fractures, at Sanford Underground Research Facility (SURF) in Lead, South Dakota (Chai et al., 2019; Chen et al., 2019; Frash et al., 2019; Fu et al., 2019; Lu and Ghassemi, 2019; Mattson et al., 2019; White et al., 2019; Wu et al., 2019). The first experiment, Experiment 1, was performed to create a hydraulic fracture that connects an injection and production well, with a scale around 10-20 meters. The temperature of the testbed is around 30 °C, which is not an ideal temperature for developing geothermal system, but this field site has been well studied before with a substantial source of data ready to be used for scientific research (Oldenburg et al., 2016).

Experiment 1 was conducted at 4,850 level (4,850 ft deep) and eight wells of around 60 m length were drilled sub-horizontally. One of the wells (E1-I) was used to stimulate the reservoir and create hydraulic fractures, another was the production well (E1-P) and all the other

[2] J. Ajo-Franklin, S.J. Bauer, T. Baumgartner, K. Beckers, D. Blankenship, A. Bonneville, L. Boyd, S. Brown, S.T. Brown, J.A. Burghardt, T. Chen, Y. Chen, K. Condon, P.J. Cook, D. Crandall, P.F. Dobson, T. Doe, C.A. Doughty, D. Elsworth, J. Feldman, A. Foris, L.P. Frash, Z. Frone, P. Fu, K. Gao, A. Ghassemi, H. Gudmundsdottir, Y. Guglielmi, G. Guthrie, B. Haimson, A. Hawkins, J. Heise, M. Horn, R.N. Horne, J. Horner, M. Hu, H. Huang, L. Huang, K.J. Im, M. Ingraham, R.S. Jayne, T.C. Johnson, B. Johnston, S. Karra, K. Kim, D.K. King, T. Kneafsey, H. Knox, J. Knox, D. Kumar, K. Kutun, M. Lee, K. Li, R. Lopez, M. Maceira, P. Mackey, N. Makedonska, C.J. Marone, E. Mattson, M.W. McClure, J. McLennan, T. McLing, C. Medler, R.J. Mellors, E. Metcalfe, J. Miskimins, J. Moore, J.P. Morris, S. Nakagawa, G. Neupane, G. Newman, A. Nieto, C.M. Oldenburg, W. Pan, T. Paronish, R. Pawar, P. Petrov, B. Pietzyk, R. Podgorney, Y. Polsky, J. Popejoy S. Porse, B.Q. Roberts, M. Robertson, W. Roggenthen, J. Rutqvist, D. Rynders, H. Santos-Villalobos, M. Schoenball, P. Schwering, V. Sesetty, C.S. Sherman, A. Singh, M.M. Smith, H. Sone, F.A. Soom, C.E. Strickland, J. Su, D. Templeton, J.N. Thomle, C. Ulrich, N. Uzunlar, A. Vachaparampil, C.A. Valladao, W. Vandermeer, G. Vandine, D. Vardiman, V.R. Vermeul, J.L. Wagoner, H.F. Wang, J. Weers, J. White, M.D. White, P. Winterfeld, T. Wood, S. Workman, H. Wu, Y.S. Wu, Y. Wu, E.C. Yildirim, Y. Zhang, Y.Q. Zhang, J. Zhou, Q. Zhou, M.D. Zoback

six wells (E1-OT, E1-OB, E1-PST, E1-PSB, E1-PDT and E1-PDB) were monitor wells. The schematic illustration of the wells and fractures is shown in Figure 1. Each well has been cored and characterized using various tools for measurement and monitoring. Pressure and flow rate are also measured and logged at different locations along the injection, production, and observation well. After the fracture was stimulated by injecting water at different flow rate in three phases, it was confirmed that the fracture has been driven to the production well (E1-P). Tracer and flow tests were conducted and the outflow from several monitoring wells (E1-OT, E1-PST, and E1-PSB) proves that stimulated fracture is connected to activated natural fracture system. There are quite a few studies that contributed to characterizing the geometry of the fracture system including both hydraulic and natural fractures, using micro-seismicity (Chen et al., 2019; Schoenball et al., 2019) or discrete fracture network (Lu and Ghassemi, 2019; Neupane et al., 2019; White et al., 2019). It can be seen that a lot of uncertainty is associated with the interpretation of the fracture geometry, aperture, permeability and distribution. The conceptual model for fracture geometry used in this study, referred from Beckers et al. (2020), is shown in Figure 2. The fracture geometry, ideally, should be a penny shaped disk. Due to the uncertainty, it has been simplified to rectangular shape without losing the match with micro-seismicity cloud. PDT-OT natural fracture is added because of the observation of Distributed Temperature Sensing (DTS) data and OT-P connector is included as an interpreted deep fracture zone (Neupane et al., 2019; Singh et al., 2019) interconnected with the hydraulic fracture and the production out of EI-OT well. Two production locations E1-PB and E1-PI represent two intersections of E1-P with hydraulic fracture and natural fracture.

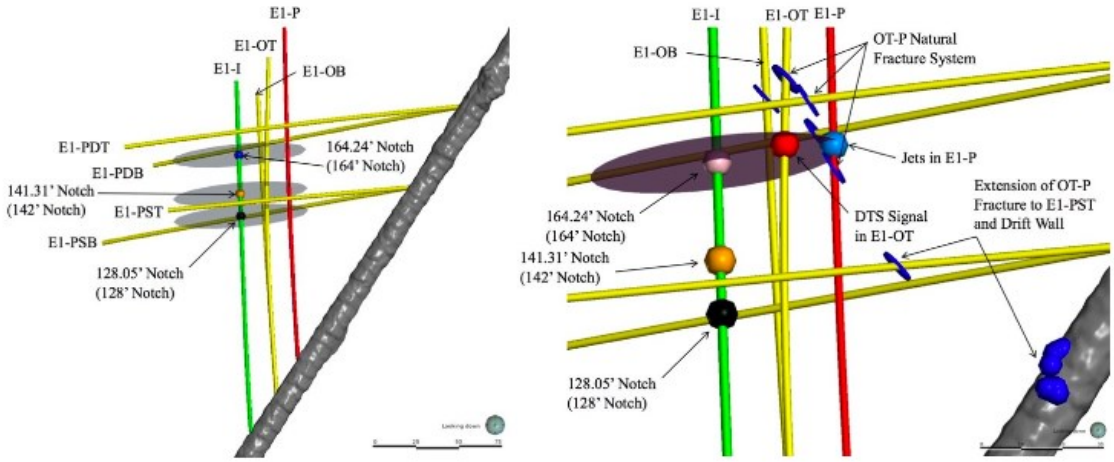

Figure 1 Schematic of injection/production/monitor wells of testbed. Green (E1-I) is injection well, also for stimulating hydraulic fractures and red (E1-P) is production well. Yellow are monitor wells. The hydraulic fracture is illustrated with the mark '164 Notch' (White et al., 2019).

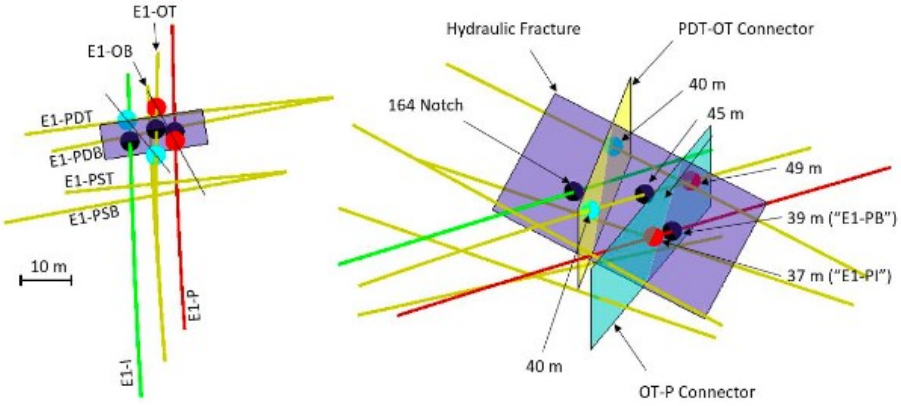

Figure 2 Conceptual model for fluid flow in fractures: purple plane represents the hydraulic fracture and the yellow and blue planes are natural fractures. Green and red lines are injection and production wells respectively. Yellow lines are all monitoring wells (Beckers et al., 2020)

The comprehensive data collection, including temperature sensing, fracture characterization and flow rate measurement, in EGS Collab provides a platform for numerical simulation to model this coupled Thermal-Hydrologic-Mechanical process. Numerical simulators and coupled models can be improved at the same time for future application on EGS development. Numerical modeling is an essential part of both design and research in EGS Collab (White et al., 2019), which will be used for validating tracer transport, flow tests, and heat transfer in fractures or fracture networks. Starting from May 8th 2019, a thermal circulation test injected cold water (12 °C) into the injection well E1-I with the flow rate of 400 ml/min. The production temperature was incorrectly measured during the period from May to December,

but it has been confirmed that the production temperature of E1-PI and E1-PB in December 2019 and January 2020 is approximately 30 °C. The flow rates of several wells (E1-PI, E1-PB, PST, PDT) are shown in Figure 3.

In this study, based on the measurement of endpoint temperature, flow rate and injection pressure, various models are generated to investigate possible subsurface conditions. Substantial possibilities were examined, and simulations were run accordingly to observe the results. An important objective of modeling is of course to honor the measured data, but beyond that, more input conditions were modeled to better understand the fracture and fluid flow. TOUGH2-THM, a simulator of fully coupled model for THM process with Embedded Discrete Fracture Model (EDFM) will be adopted to model the thermal circulation test. A coupled model is essential because geomechanics often plays an important role in modifying fracture permeability (McDermott and Kolditz, 2006; Wang et al., 2016; Yu et al., 2019). Some common approaches to coupling fluid/heat flow with geomechanics include using two software modules (Rutqvist et al., 2002; Rutqvist, 2011) computing fluid flow and geomechanics respectively, or sequentially or iteratively coupling finite difference fluid flow module with finite element geomechanics module (Settari and Walters, 2001; Tran et al., 2004; Kim et al., 2009; Kim and Moridis, 2013). A new approach of fully coupling using Integral Finite Difference method (IFD) was introduced by (Winterfeld and Wu, 2012; Hu et al., 2013; Yu et al., 2019). TOUGH2-THM used in this study is developed on a massively parallel framework, TOUGH2-MP (Zhang et al., 2001; Wu et al., 2002) and TOUGH2-CSM (Winterfeld and Wu, 2016) so that it can handle a relatively large-scale or high-resolution model. On the other hand, EDFM will be used to handle the hydraulic and natural fractures. EDFM is deemed to be efficient in modeling fluid flow in fractures (Lee et al., 2001; Moinfar et al., 2012; Xu et al., 2017; Wang et al., 2019), especially in capturing the fracture-matrix interaction in low-permeability reservoir, such as shale or geothermal reservoirs. EDFM has been integrated with THM model for simulating fracture permeability response to geomechanics and thermal stress in Yu et al. (2019). This simulator will be applied here in this study to model the thermal circulation test at EGS Collab.

The structure of this paper will be as follows: first, the numerical method used in TOUGH2-THM and EDFM will be briefly revisited. Then a simple model with a single hydraulic fracture will be simulated as a guide for three fracture case. Various models with distinct parameters will be studied. The following section will give results of simulating a three-fracture model with similar model inputs and include discussion of what factor could be important for production temperature and flow rate. Finally, a summary and future work will be presented.

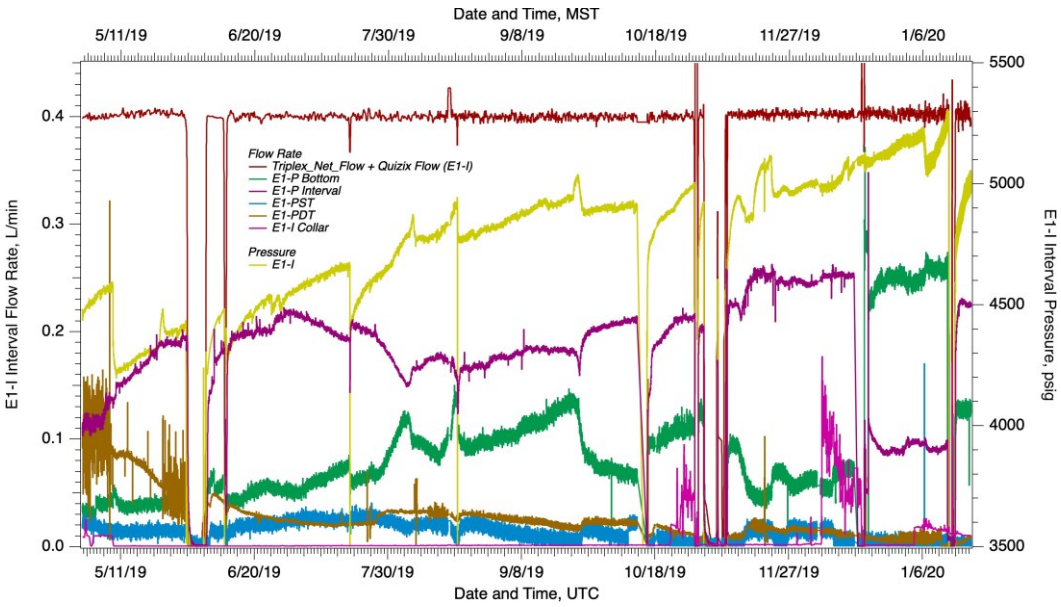

Figure 3 Flow rate measurement during the thermal circulation test for well E1-I, E1-PI, EI-PB, PST and PDT (EGS Collab Team)

2. COUPLED MODEL OF THM AND EDFM FOR GEOTHERMAL RESERVOIRS

Details of mathematical fundamentals and numerical methods for coupled THM model and the EDFM can be found in Yu et al. (2019). In this section, for the completeness of the paper and assisting readers' understanding the following simulation, they will be briefly introduced. The Thermal-Hydrologic part of the coupled model is completely originated from TOUGH2-MP, solving the mass and energy balance equation by discretizing the governing partial differential equation (PDE) in time and space. The Mechanical part has the same fundamental basis as TOUGH2-CSM where thermo-poro-elastic Navier equation is transformed into Beltrami-Michell equations and stresses are solved using the IFD approach. This way of solving mechanical equation can save the effort of altering the original program structure and is suitable for small deformation problem. The EDFM approach is essentially inserting fracture plane into reservoir and calculating the geometrical parameters for connections between fracture and matrix grid. Program for EDFM was developed separately with the simulation to generate a mesh file for modeling input. In the coupled model, the embedded discrete fracture grid is assumed to have the same stress state with its embedding matrix grid and the normal stress is treated as a second parameter which results in a permeability and porosity change. In this section, the mathematical fundamentals and numerical methods for coupled model will be explained, followed by the EDFM and the approach of integrating EDFM with THM model.

2.1 Governing Equations of Coupled THM Models

Mass and energy balance equations can be expressed in the following PDE form:

$$\frac{d}{dt}M^k = -\nabla \cdot \overrightarrow{F^k} + q^k \tag{1}$$

where M^k, $\overrightarrow{F^k}$ and Q^k represent accumulation term, flux term and sink/source term of κ_{th} mass component respectively. Accumulation term gives the mass and energy currently stored at a time step for component κ and phase β:

$$M^k = \phi \sum_\beta S_\beta \rho_\beta X_\beta^k \tag{2}$$

$$M^{NK+1} = (1-\phi)\rho_R C_R T + \phi \sum_\beta S_\beta \rho_\beta u_\beta \tag{3}$$

in which ρ_R and C_R is the rock density and rock specific heat, T is the temperature and u_β is the specific internal energy of phase β. Flow term for mass component in a specific phase is computed by Darcy's law. Heat conduction and convection are both considered in the flow term:

$$\overrightarrow{F_\beta} = \rho_\beta \overrightarrow{u_\beta} = -k\frac{k_{r\beta}\rho_\beta}{\mu_\beta}\left(\nabla P_\beta - \rho_\beta \vec{g}\right) \tag{4}$$

$$\vec{F}^{NK+1} = -\lambda \nabla T + \sum_\beta h_\beta \overrightarrow{F_\beta} \tag{5}$$

In the phase flux equation, $\overrightarrow{u_\beta}$ is the Darcy velocity of phase β, k is the absolute permeability, $k_{r\beta}$ is the relative permeability of phase β, μ_β is viscosity of phase β, and the phase pressure is P_β, In equation (5) for heat transfer, λ is the thermal conductivity and h_β is the specific enthalpy in phase β.

Well injection or production is modeled by a sink/source term, q^k. For a constant flow rate injection, q^k is a mass flow rate term whereas for a constant pressure production, the sink term can be calculated as:

$$q_\beta = \frac{k_{r\beta}}{\mu_\beta}\rho_\beta \cdot PI \cdot (P_\beta - P_{wb}) \tag{6}$$

where PI is the productivity index that can be input by a user.

Geomechanical governing equation starts from linear elasticity, Hook's law with consideration of thermal and pore pressure effect. Combined with static equilibrium, this leads to the thermo-poro-elastic Navier equation:

$$\nabla[h(P,T)] + (\lambda + G)\nabla(\nabla \cdot \vec{u}) + G\nabla^2\vec{u} + \overline{F_b} = 0 \tag{7}$$

where $h(P,T)$ is a term for pore pressure and thermal stress. $\vec{u}$ is the displacement vector and λ and G are Lame parameters.

Take divergence of equation (7) so that the displacement vector can be substituted by the stress through stress-strain relation and the following equation can be obtained:

$$\frac{3(1-\nu)}{1+\nu}\nabla^2\tau_m + \nabla \cdot \overline{F_b} - \frac{2(1-2\nu)}{1+\nu}\nabla^2[h(P,T)] = 0 \tag{8}$$

Equation (7) can be further decomposed to the Beltrami-Mitchell equations (Winterfeld and Wu, 2016) for all stress tensor components. Take principal stress in x direction as an example (components of other directions and shear stresses have similar forms (Yu et al., 2019)):

$$\frac{\partial^2}{\partial x^2}[h(P,T)] + \frac{3}{2(1+\nu)}\frac{\partial^2}{\partial x^2}(\tau_m - h(P,T)) + \frac{1}{2}\nabla^2\left(\tau_{xx} - h(P,T) - \frac{3\nu}{1+\nu}(\tau_m - h(P,T))\right) + \frac{\partial}{\partial x}F_{b,x} = 0 \tag{9}$$

Both equation (8) and (9) have similar form with the governing equation (1) (after plugging equation (4-5) into equation (1) in terms of pressure) so that these mechanical equations can be handled by the same numerical approach as that for fluid flow and heat transfer.

2.2 Numerical Approach for Discretization and Solution

IFD and fully implicit backward Finite Difference (FD) method were applied to discretize space and time. Applying IFD and FD to equation (1), a general form can be obtained:

$$\frac{d}{dt}\int_{V_n} M^k dV_n = \int_{\Gamma_n} \overrightarrow{F^k} \cdot \vec{n} d\Gamma_n + \int_{V_n} q^k dV_n \tag{10}$$

Equation (10) can be rewritten in a discretized form:

$$\frac{d}{dt}\left(M_n^k V_{n,0}\left(1-\varepsilon_{v,n}\right)\right) = \sum_m A_{nm,0}(1-\varepsilon_{A,nm})F_{nm}^k + q_n^k V_{n,0}(1-\varepsilon_{v,n}) \tag{11}$$

in which $V_{n,0}$ is the grid block area at zero strain, $A_{nm,0}$ is the contact area at zero strain between the n[th] grid block of interest and its neighbor, m[th] grid block, F_{nm}^{k} is the flux between n[th] grid block and m[th] grid block, $\varepsilon_{v,n}$ is the volumetric strain and $\varepsilon_{A,nm}$ is the weighted area strain, both calculated from x, y and z normal strains. The flow term can be written in a discretized form as well:

$$A_{nm}F_{nm}^{k} = \sum_{\beta} -k_{nm}\left(\frac{k_{r\beta}\rho_{\beta}X_{\beta}^{k}}{\mu_{\beta}}\right)_{nm}\left(\frac{P_n+P_{c\beta,n}-P_m-P_{c\beta,m}}{D_{n,0}(1-\varepsilon_{D,n})+D_{m,0}(1-\varepsilon_{D,m})}-\rho_{\beta,nm}g_{nm}\right)A_{nm,0}(1-\varepsilon_{A,nm}) \tag{12}$$

where $D_{n,0}$ and $D_{m,0}$ are distance from the center of the grid block n and m to their common interface, $A_{nm,0}$ is the interface area. $k_{nm}\left(\frac{k_{r\beta}\rho_{\beta}X_{\beta}^{k}}{\mu_{\beta}}\right)_{nm}$ is a weighted term evaluated by a specified weighting approach.

Equation (8) and (9) can be discretized but with a slightly different form aiming to take heterogenous rock properties into consideration. They can be written in a manner called flux and interface approach. Without accumulation or sink/source term, equation (10) becomes:

$$\int_{\Gamma_n}\overrightarrow{F^{NK+2}}\cdot\vec{n}d\Gamma_n = 0 \tag{13}$$

in which

$$\overrightarrow{F^{NK+2}} = \frac{3(1-\nu)}{1+\nu}\nabla\tau_m + \overrightarrow{F_b} - \frac{2(1-2\nu)}{1+\nu}\nabla[h(P,T)] \tag{14}$$

for mean stress and this is also known as flux term for stress across the grid interface. Assume that the stress at the grid interface is $\tau_{m,int}$, then the flux can be solved by establishing two flux terms on both sides of the interface:

$$\Psi_{\tau} = \frac{\left\{\begin{matrix}\tau_{m,+}-\tau_{m,-}+\frac{s_+(1+\nu_+)}{3(1-\nu_+)}F_{b,+}+\frac{s_-(1+\nu_-)}{3(1-\nu_-)}F_{b,-}\\ -\frac{2(1-2\nu_+)}{3(1-\nu_+)}\left(h(P,T)_+-h(P,T)_{+,int}\right)-\frac{2(1-2\nu_-)}{3(1-\nu_-)}\left(h(P,T)_{-,int}-h(P,T)_-\right)\end{matrix}\right\}}{\frac{s_+(1+\nu_+)}{3(1-\nu_+)}+\frac{s_-(1+\nu_-)}{3(1-\nu_-)}} \tag{15}$$

where + and – represent two grids across the interface respectively and s_+ and s_- are used to replace D_m and D_n for a general description of two-grid connection. $h(P,T)_{int,+}$ and $h(P,T)_{int,-}$ are two thermal and pressure terms evaluated at two sides of the interface. All stress components can be discretized using the same approach. Take stress in x direction as an example:

$$\Psi_{xx} = \frac{\left\{\begin{matrix}\tau_{xx,+}-\tau_{xx,-}\\ +2s_+F_{b,x+}+2s_-F_{b,x-}-\frac{3\nu_+}{1+\nu_+}\left(\tau_{m,+}-\tau_{m,int}\right)-\frac{3\nu_-}{1+\nu_-}\left(\tau_{m,int}-\tau_{m,-}\right)\\ +\frac{3s_+}{1+\nu_+}\frac{\tau_{m,+}-\tau_{m,int}}{x_+}+\frac{3s_-}{1+\nu_-}\frac{\tau_{m,int}-\tau_{m,-}}{x_-}\\ +\frac{2\nu_+-1}{1-\nu_+}\left(h(P,T)_+-h(P,T)_{+,int}\right)+s_+\frac{2\nu_+-1}{1-\nu_+}\frac{h(P,T)_+-h(P,T)_{+,int}}{x_+}\\ +\frac{2\nu_--1}{1-\nu_-}\left(h(P,T)_{-,int}-h(P,T)_-\right)+s_-\frac{2\nu_--1}{1-\nu_-}\frac{h(P,T)_{-,int}-h(P,T)_-}{x_-}\end{matrix}\right\}}{\frac{s_+(1+\nu_+)}{3(1-\nu_+)}+\frac{s_-(1+\nu_-)}{3(1-\nu_-)}} \tag{16}$$

Equation (16) illustrates that interface mean stress facilitates the computation of x-direction normal stress flux and so does interface pressure and temperature. In TOUGH2-CSM and TOUGH2-THM, interface quantities are updated at each Newton iteration level for stress flux assemblage.

After coupling fluid/heat flow and geomechanics, the primary variables are pressure, temperature, saturation and six stress tensor components. All primary variables compose a nonlinear system which need to be solved. This non-linear system, mass and energy balance equation and mechanical equation discretized by IFD, can be solved fully implicitly in time after spatial discretization, by the approach known as Newton's method. The program iterates to compute residual equation within a timestep until convergence when residual is small enough.

2.3 Embedded Discrete Fracture Model and its Coupling with Geomechanics

Discrete fracture planes are embedded into the matrix mesh grids which cut the fracture plane into small polygons. Connection relations are established between fracture and matrix, as well as between fracture and fracture. Fracture polygons, which are geometrically constructed by computing the polygon vertices, are treated as normal grids in fluid/heat flow simulator. This is the algorithmic fundamentals of EDFM. Original ideas stemmed from Lee et al. (2001) and were extended by Moinfar (2013) and Xu et al. (2017). They applied this methodology for modeling IOR/EOR from tight oil/gas reservoirs. Yu et al. (2019) validated the application of EDFM in coupled fluid/heat flow in geothermal reservoirs and also proposed an approach to couple fluid/heat flow and geomechanics with EDFM. This method will be adopted in this study and briefly explained in this subsection.

As shown in Figure 4, imagine there are two fracture planes that are embedded into a reservoir which has been partitioned into Cartesian mesh grid blocks. In one of the Cartesian grid block, two fractures are cut into polygons as shown in this figure. These two polygons are connected with the matrix grid block and also connected with each other as well. EDFM is capable of building a mesh that takes all fracture grids and additional connections generated by the embedment into consideration. Basic steps to establishing this new mesh are demonstrated in Wang (2018) and Yu et al. (2019).

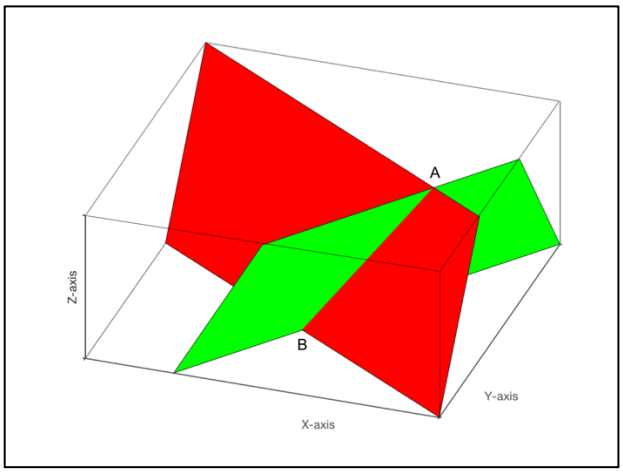

Figure 4 Two fractures (green and red) are cut by a grid block and two polygons are generated for fracture grids.

To couple the EDFM with THM model, an essential assumption made in this study is that fracture grids share the same stress components with its embedding matrix blocks. For example, the green and red fracture polygons have the same stress state with the box. This indicates that during Newton's iteration, the Jacobian matrix coefficients in terms of stresses for fracture grid blocks are the same with those for matrix grid blocks. Accordingly, the total stress acting on the fracture plane, treated as a secondary parameter can be computed using the following equation:

$$\tau_{z'z'} = l_{31}^2\tau_{xx} + l_{32}^2\tau_{yy} + l_{33}^2\tau_{zz} + 2l_{31}l_{32}\tau_{xy} + 2l_{31}l_{33}\tau_{xz} + 2l_{32}l_{33}\tau_{yz} \tag{17}$$

where subscript $z'z'$ is the normal direction of fracture face after stress transformation, and l_{31}, l_{32} and l_{33} are related with the longitudinal (λ) and zenith angles (θ) of coordinate transformation:

$$l_{31} = sin\,\theta\,cos\,\lambda\ , l_{32} = sin\,\theta\,sin\,\lambda\ , l_{33} = cos\,\theta \tag{18}$$

It can be seen that normal stress on fracture is dependent on normal stresses and shear stresses of the matrix grid block, which also explains the reason of extending the primary variable list. Normal stresses on fracture plane can be further used to compute effective stress that would modify the aperture of the fracture:

$$\tau_n' = \tau_{z'z'} - \alpha_f P_f + \tau_{thermal} \tag{19}$$

where thermal stress is calculated by:

$$\tau_{thermal} = 3\beta_m K_m (T_f - T_{fi}) \tag{20}$$

If $\beta_m = 8e-6\ \frac{1}{C}$ and $K_m = 40\ GPa$, per one degree of temperature decrease, the thermal stress created on the fracture would be 9.6e5 Pa which is a significant impact on fracture permeability. The permeability modifier, as a function of fracture aperture, used in this study is referred from Rutqvist et al. (2002) and Min et al. (2004):

$$b = b_i + \Delta b = b_i + b_{max}(e^{-d\tau_n'} - e^{-d\tau_{ni}'}) \tag{21}$$

in which b is the current aperture under normal effective stress τ_n', b_i is the initial aperture under the initial normal effective stress τ_{ni}', b_{max} is the maximum aperture that can be reached, d is a coefficient measured by laboratory. Since the permeability of fracture is linearly dependent on the square of fracture aperture, permeability and porosity can be computed by:

$$k_f = \frac{b^2}{b_i^2}k_i \tag{22}$$

$$\phi_f = \frac{b}{b_i}\phi_i \tag{23}$$

where subscript i indicates initial condition value at initial stress states.

Besides fracture, porosity and permeability of matrix grid blocks are also functions of stresses or strains. These parameters are all secondary parameters computed in Newton's iteration. In this study, porosity can be calculated by (Gutierrez et al., 2001):

$$\phi = 1 - \frac{1-\phi_r}{\left(\frac{1-\varepsilon_v}{1-\varepsilon_{v,r}}\right)} \tag{24}$$

$$\frac{1-\phi}{1-\phi_i} = \frac{1-\varepsilon_{v,i}}{1-\varepsilon_v} \tag{25}$$

in which ϕ_r and $\varepsilon_{v,r}$ are residual porosity and volumetric strain. Through equation (25), current porosity can be calculated by initial ($\varepsilon_{v,i}$) and current volumetric strain. Permeability can be calculated by (Rutqvist et al., 2002):

$$k = k_0 e^{c\left(\frac{\phi}{\phi_0}-1\right)} \tag{26}$$

The grid block dimensions are also affected by stress and strain. It is intuitive to consider the impact on fluid/heat flow because connection relation between grid blocks depends on interface area and distance. These calculations are elaborated in Yu et al. (2019).

3. APPLICATION OF COUPLED THM MODEL FOR THERMAL CIRCULATION TEST AT EGS COLLAB

Although the fracture system at EGS Collab testbed has been investigated and characterized by a lot of techniques, their results still reflect a significant amount of uncertainties in terms of fracture shape, aperture and permeability, natural fracture distribution, and boundary conditions. The data without much uncertainty is the measurement and monitoring of the thermal circulation tests, including flow rate out of multiple wells, injection pressure, and end-point temperature. In this section, taking these uncertainties into account, we start from a simple one hydraulic fracture model without any natural fracture and investigate what factors could potentially impact production temperature, injection pressure, and flow rate. Afterwards, a three-fracture system including one hydraulic fracture and two natural fractures are created and modeled with various similar conditions. The factors under investigations are: (1) fracture permeability and heterogeneity; (2) boundary conditions such as first-type or closed boundary; (3) geomechanical effect on fracture and matrix; (4) thermal conductivity of rock matrix; (5) production index of wells; and (6) existence of natural fracture system activated by stimulation.

3.1 One Hydraulic Fracture Model

The reason of modeling this one fracture model is that it is desirable to use a simple model to investigate different factors first because this is relatively efficient in terms of computation. The model we created is shown in Figure 5. The dimension of the reservoir is 19.2 meters by 9.5 meters by 7.9 meters. Injection and production, as shown in the figure, are into and from fracture grid using sink/source term as described in Equation (1) and (6). Fractures are around 10 meters in length and 4 meters in height. Injection rate is constant to be 400 ml/min and injection temperature is 30 days of 30 °C and followed by 170 days of 12 °C. The two-stage injection temperature follows the real injection history and also aims to test if the short period injection of warm fluid would influence the result. Input parameters are shown in Table 1.

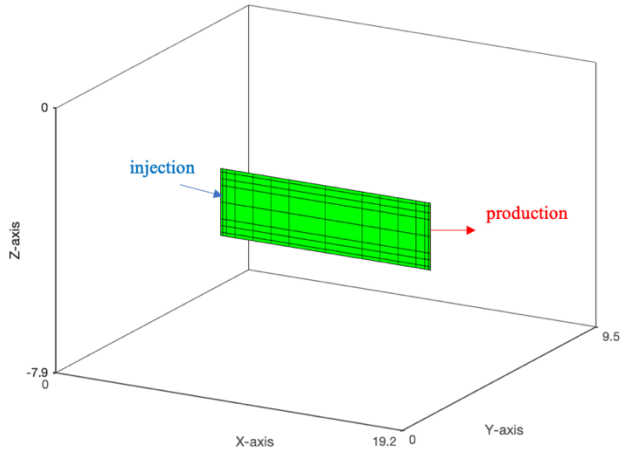

Figure 5 Embedded discrete fracture and the matrix dimension. The matrix grid blocks are invisible here to better illustrate the embedded fracture.

Table 1 Basic Input Parameters for One Fracture Model

Parameters	Value	Unit
Matrix porosity	0.01	Unitless
Matrix Permeability	1e-18	m^2
Matrix thermal conductivity	5.0	W/m °C

Matrix specific heat	805	J/kg °C
Fracture porosity	0.1	Unitless
Fracture permeability	8e-10	m^2
Fracture Aperture	1e-5	m
Well productivity index	1e-10	m^3
Production pressure	1.0	MPa
Initial reservoir pressure	8.3	MPa
Initial reservoir temperature	31	°C
Injection temperature	30 (30 days)/12 (170 days)	°C
Injection flow rate	400	ml/min

3.1.1 Permeability of Fracture

The first thing we would like to study is the effect of permeability of fractures on production temperature and flow rates. Hydraulic fracture is usually regarded as a penny shape disk, which indicates that the aperture decreases from the center towards the periphery. To honor this condition, the fracture permeability has been partitioned into 8 layers each with different porosity and permeability, center layer (4 th layer which injection/production occurs): 0.1, 8e-10 m^2, second layer away from center (3rd and 5th layer): 0.05, 4e-11 m^2, third layer away from center (2nd and 6th layer): 0.02, 2e-12 m^2, fourth layer away from center (1st, 7th and 8th layer): 0.01, 1e-13 m^2. An unexpected observation on injection pressure, as shown in Figure 3, is the increasing of injection pressure around 4,500-5,000 psi. It might be due to the skin effect which results from the damage around the injection borehole. Consequently, on the base of layered fracture porosity and permeability, the fracture grid blocks surrounding injection point were set with permeability of 4e-14 m^2.

Results of layered fracture permeability and injection 'barrier' models are shown in Figure 6, including production temperature and production flow rate. Temperature distributions in reservoir matrix and hydraulic fracture are shown in Figure 7. It can be observed that when fracture is partitioned into layers, cold water has a preferential path of flow in the high permeable layer. The low temperature front moves forward faster and farther compared to the first row in Figure 7. At the same time, temperature decrease of matrix around injection point is slowed down if fracture has a layered permeability. The high injection pressure (2.3e7 Pa=3339 psi) can be observed at injection fracture grid block when a 'barrier' around injection exists, which would also increase the pore pressure of the whole field as well, as shown in (f) of Figure 7. Production temperatures for these three cases are different and lowest temperature flows out of the well in layered permeability case because of the fastest temperature front traveling in hydraulic fracture middle layer. Production flow rate, after reaching a steady value, is around 400 ml/min for all three cases. This does not match the measurement but injection into single fracture should be all produced and the fluid from matrix into fractures would not contribute much due to the low permeability.

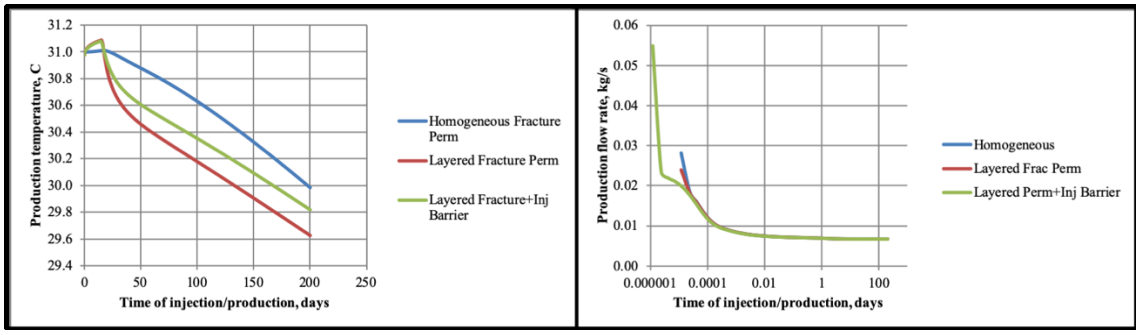

Figure 6 Production temperature and flow rate for one fracture model with different permeability conditions.

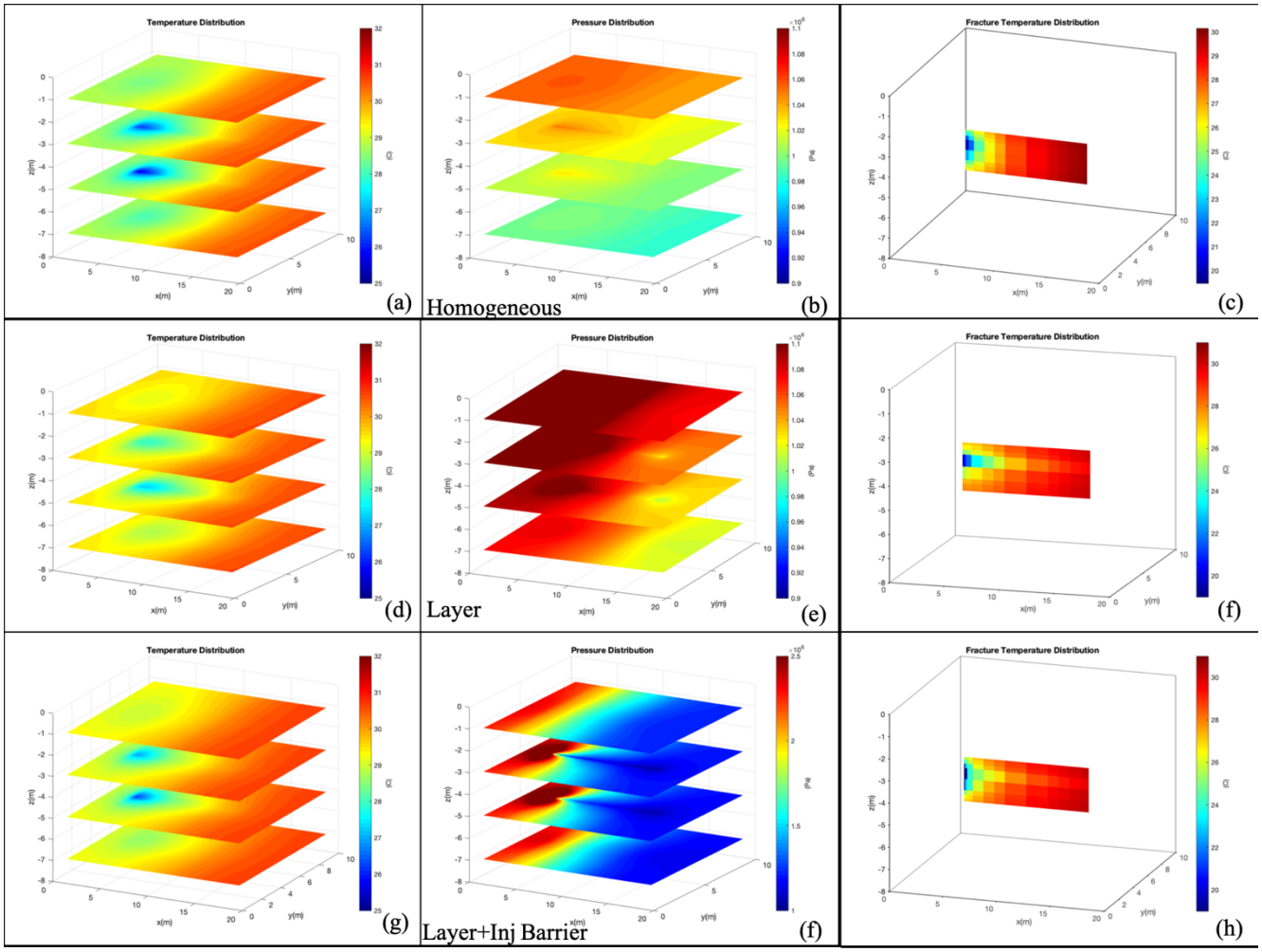

Figure 7 Temperature and pressure contour of matrix and temperature distribution in hydraulic fracture. The first, second and third row represents homogeneous permeability, layered permeability and layered permeability + injection barrier respectively. The first column is the matrix temperature, the second column is matrix pressure and third is fracture temperature. Note that for pore pressure, a different colorbar scale might be used for visualization purpose.

3.1.2 Thermal Conductivity of Rock Matrix

Heat conduction is the dominant factor to heat up the cold water in fractures, especially when reservoir matrix has a low permeability. This applies to the EGS Collab case and will be further explained later in this paper. When thermal conductivity decreases, the production temperature will be lowered down as well because the heating effect from reservoir rock on fracture fluid is reduced. Thermal conductivities of 5, 2, and 1 W/m °C were modeled and compared in Figure 8 and Figure 9. It is intuitive to expect the same observation as the modeling result. When heat conduction between fracture fluid and matrix is reduced, lower temperature will be seen in both reservoir and fracture. Production temperature will be lowered down as well. Pressure distribution and flow rate are kept unchanged compared with the base case. Note that the fracture permeability is homogeneous for each of these three cases.

3.1.3 Productivity Index of Fracture Production

Due to the uncertainty of fracture permeability and geometry, different productivity indices (PI) have been investigated as well. The results of production temperature and flow rate are shown in Figure 10. In this model, PI does not have an influence on production temperature or flow rate. The temperature and pressure distribution of matrix and fracture are the same with the first row of Figure 9.

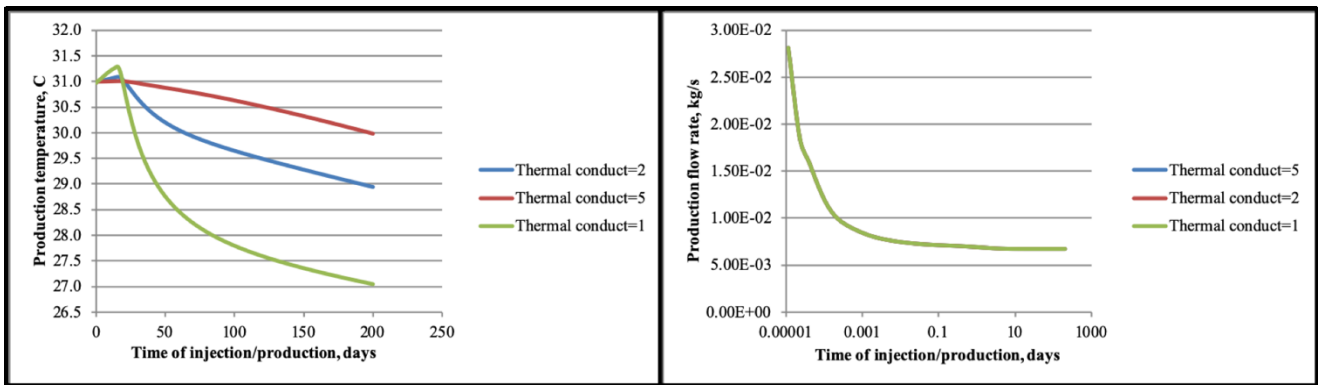

Figure 8 Production temperature and flow rate for different thermal conductivities: 5, 2 and 1 W/m °C.

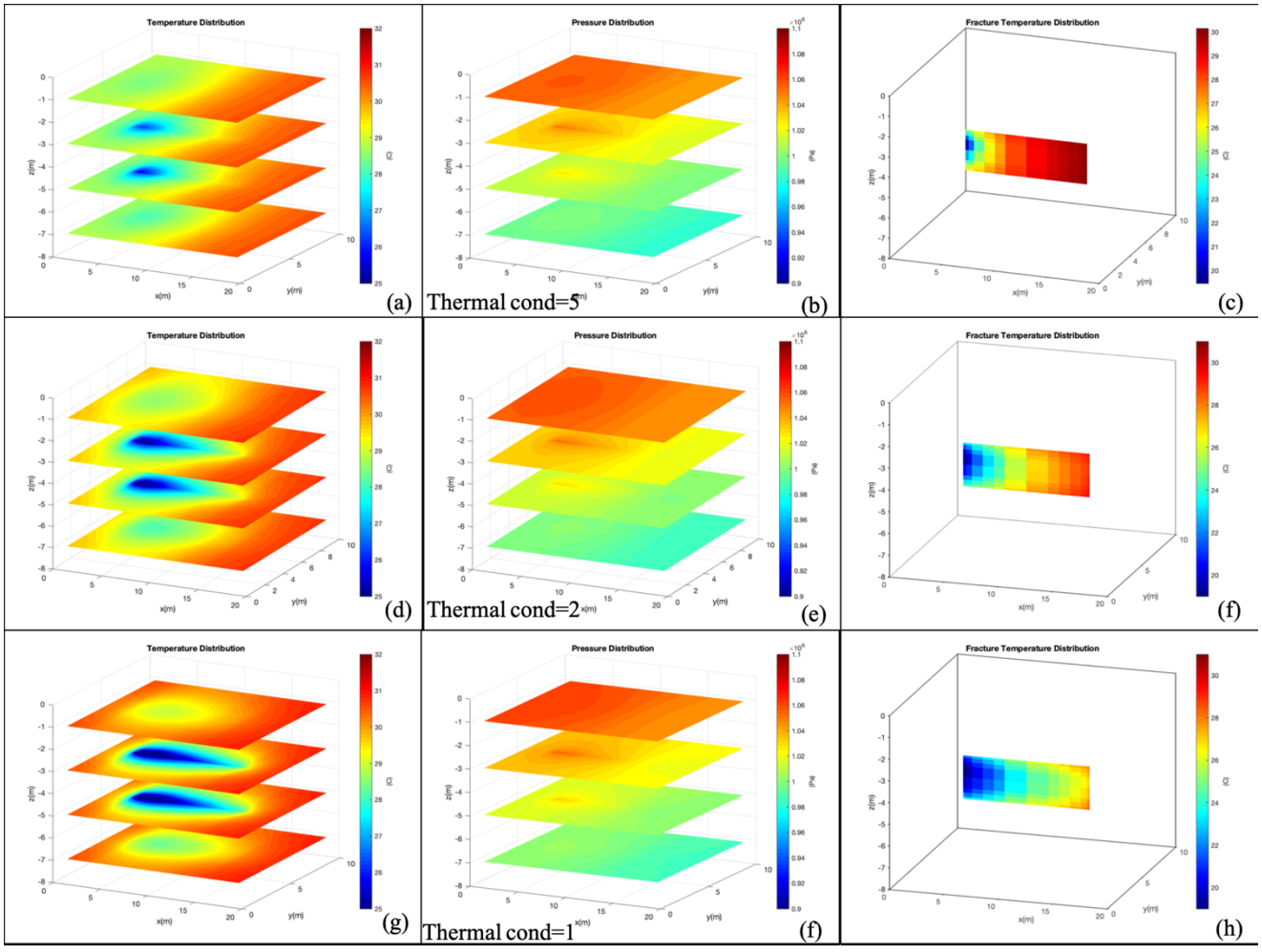

Figure 9 Temperature and pressure contour of matrix and temperature distribution in hydraulic fracture. The first, second and third row represent thermal conductivity equal to 5, 2 and 1 W/m °C respectively. The first column is the matrix temperature, the second column is matrix pressure and third is fracture temperature.

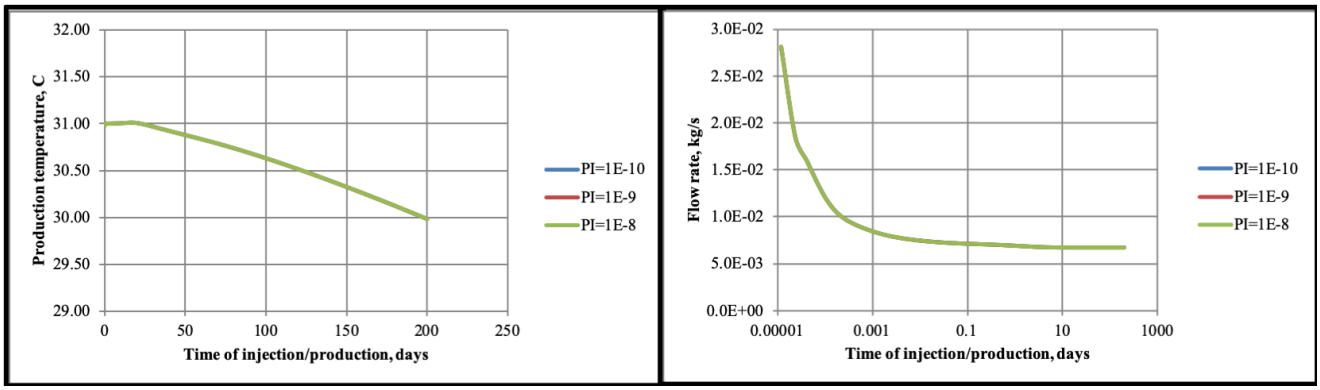

Figure 10 Production temperature and flow rate for different scenarios of productivity

3.1.4 Models with Geomechanics and Constant Pressure/Temperature Boundary Conditions

The coupled THM model introduced in Section 2 is applied here to quantify the impact of geomechanics on the overall injection/production process. The fracture porosity and permeability are functions of fracture aperture, which is dependent on effective stress as shown in Equations (21)-(23). Parameters related to geomechanics used for this case has been summarized in Table 2. The boundary condition for geomechanics is constant stress boundary and closed boundary for fluid/heat flow. On the other hand, it would be a complement to explore the condition when fluid/heat flow boundary is no longer closed since the models above are all closed boundary to fluid/heat flow. In the real subsurface condition, constant pressure might be a better assumption in some cases.

In this section, we compare the base case (layered permeability fracture), with geomechanics and constant flow boundaries. Results are shown in Figure 11 and Figure 12. It can be seen that geomechanics does not have a significant impact on fluid/heat flow for this one fracture model. Production temperature has been lowered down a bit because of the increased permeability of area around injection due to the thermal stresses, as shown in Figure 13. When geomechanical effect is amplified by modifying the aperture parameter and increase the fracture aperture even more when cold water is injected, not much difference has been observed either, as shown in Figure 11. This infers that geomechanics does not plays an essential role in this model, with the input parameters used.

Nevertheless, constant pressure/temperature does make a difference in production temperature but not in flow rate. This is because that thermal condition dominates heat transfer in this model and the fluid travels in matrix has a super slow speed that will not affect flow rate that much. But the constant temperature boundary keeps heating the whole reservoir and increases temperature. This can be confirmed by the third row of plots in Figure 12. Flow rate out of well increases to around 420 ml/min when constant pressure and temperature boundary condition is used.

Table 2 Geomechanics related input parameters

Parameter	Value	Unit
Stress xx	35.5	MPa
Stress yy	21.7	MPa
Stress zz	41.5	MPa
Matrix Young's Modulus	70	GPa
Matrix Poisson's Ratio	0.25	Unitless
c in Equation (26)	2.0	Unitless
Biot's Coefficient	1.0	Unitless
Matrix Thermal Expansion Coefficient	8e-6	1/°C
Initial fracture aperture, b_i, in Equation (21)	1.5e-5	m
Maximum fracture aperture, b_{max}, in Equation (21)	3.5e-4	m
d in Equation (21)	3.0e-7	1/Pa

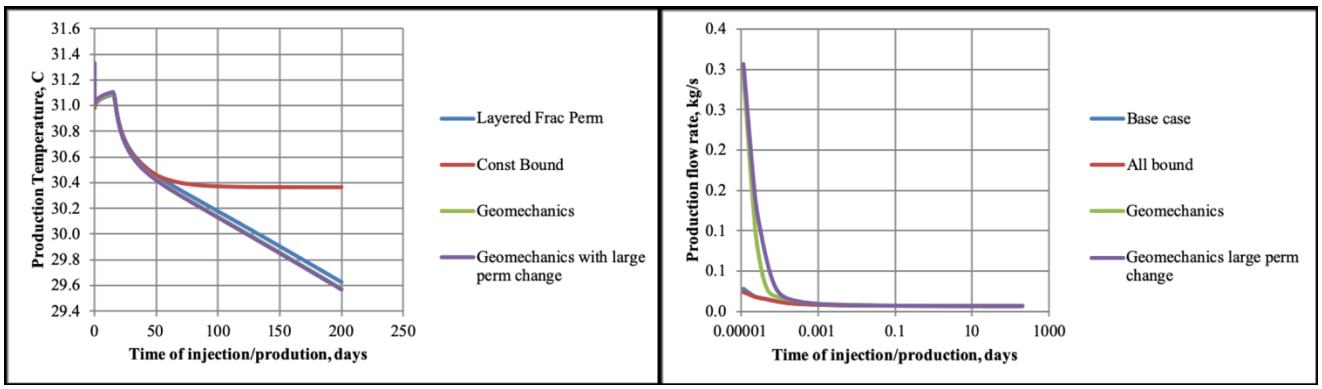

Figure 11 Production temperature and flow rate for one fracture model: no geomechanics; geomechanics; surrounding boundary conditions; larger geomechanical effect

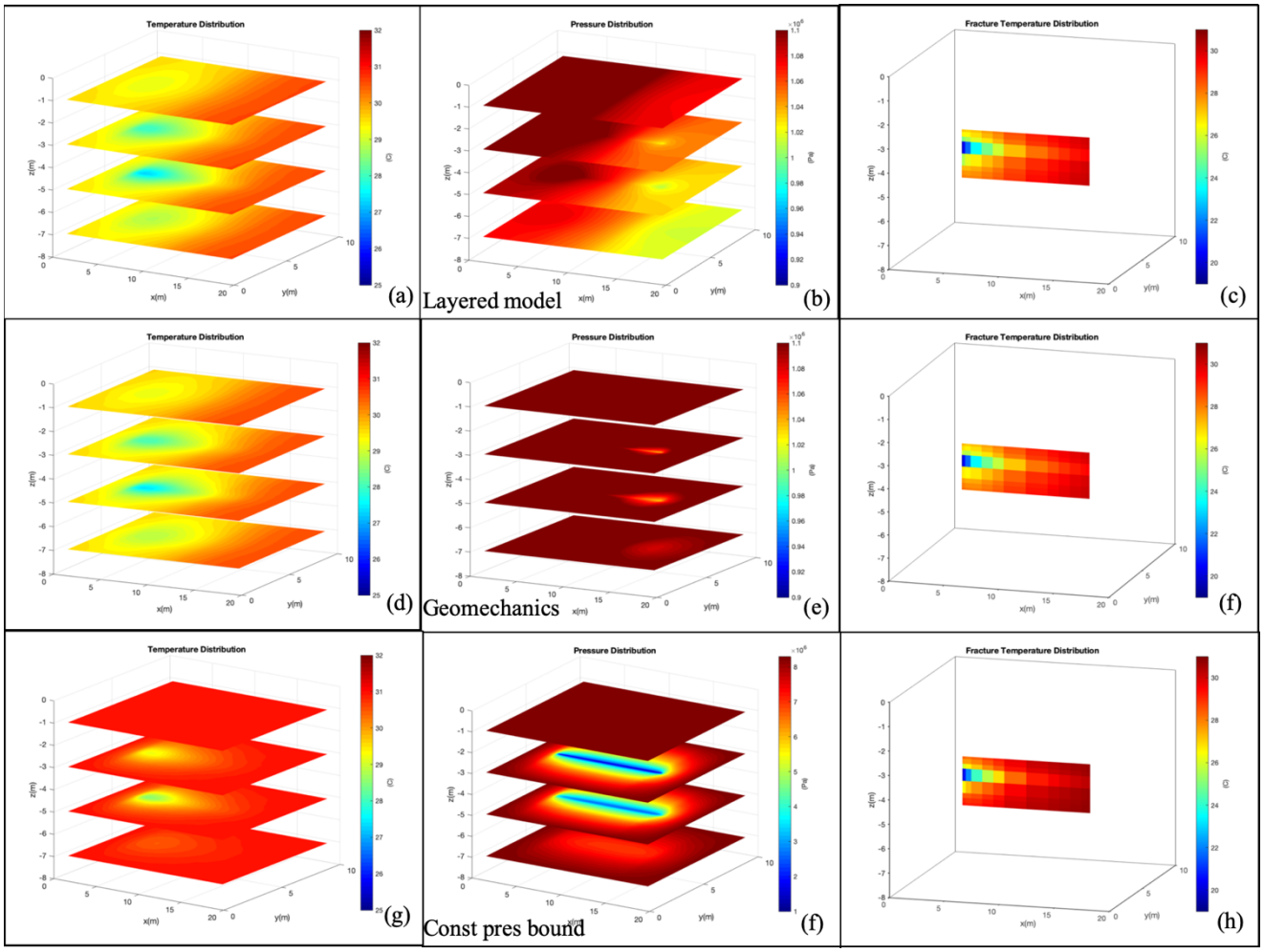

Figure 12 Temperature and pressure contour of matrix and temperature distribution in hydraulic fracture. The first, second and third row represent (1) without considering geomechanics; (2) considering geomechanics; (3) constant pressure/temperature boundary. The first column is the matrix temperature, the second column is matrix pressure and third is fracture temperature.

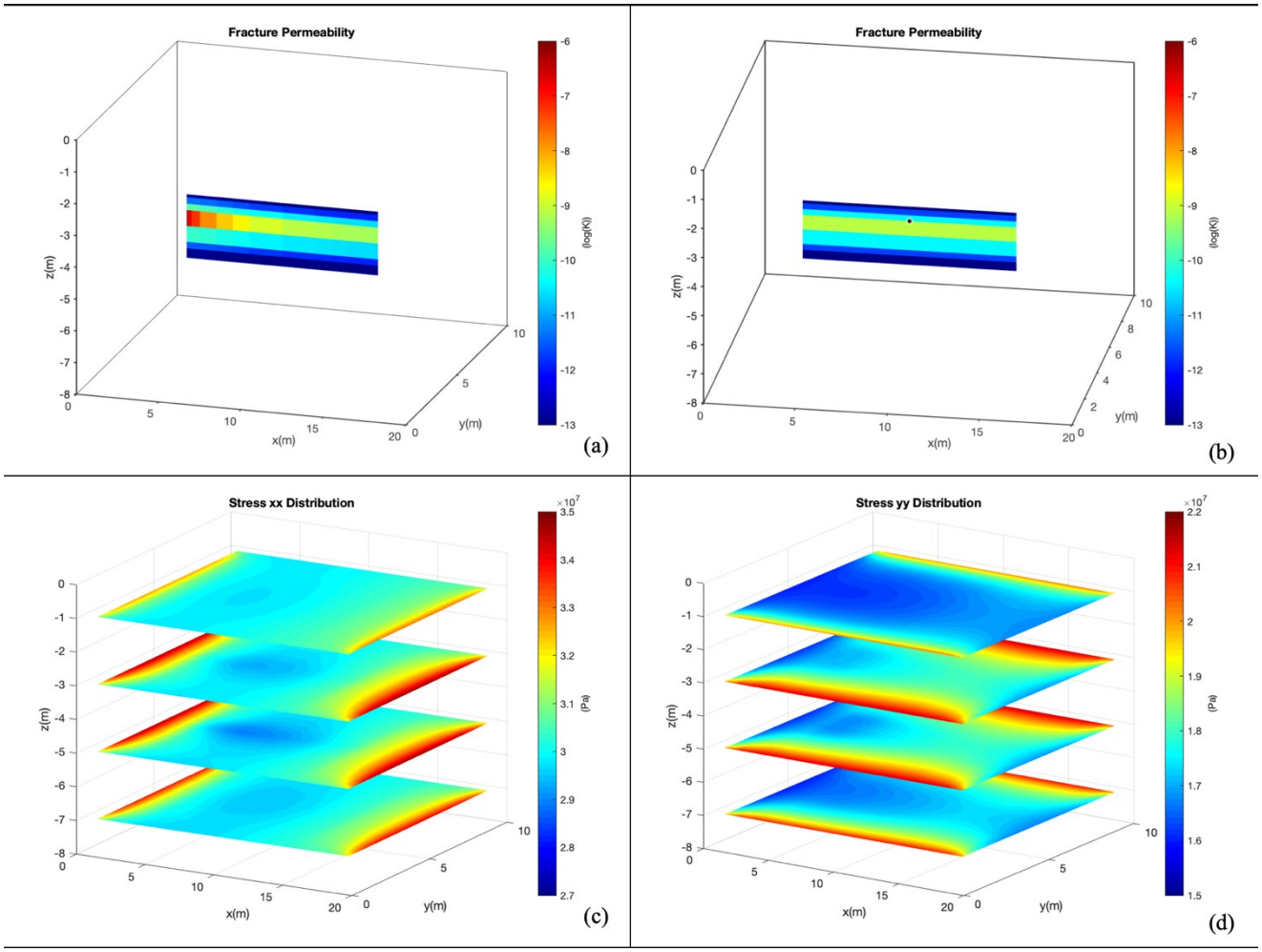

Figure 13 First row: Permeability comparison between non-geomechanics case and geomechanics case; Second row: xx and yy direction principal stresses after production.

3.2 Three-Fracture (One Hydraulic Fracture and Two Natural Fracture) Model

The one fracture model in section 3.1 provides a lot of useful implications that can be referred to for simulating a full scale three-fracture model. It can be concluded that thermal conduction dominates the heat transfer and permeability is a major impactor for production temperature and flow rate. Boundary conditions make a huge difference as well. Therefore, in this section of the three-fracture model, we will examine if these factors also impact the full field results. We will first have a look at the permeability (homogeneous, layered and all boundary surrounding the reservoir), followed by geomechanics and fracture tip boundary where we put a source of constant pressure and temperature point on natural fracture grids, lastly there would be a double-porosity model commonly used in oil and gas industry, applied to see if activated natural fracture system could influence the fluid/heat flow. The EDFM mesh is shown in Figure 14. The hydraulic fracture was partitioned into 7 layers and different rock properties can be assigned to each layer. Meanwhile, in this model, we have one injector into E1-PI and five producers from E1-PB, E1-PI, E1-PDT and E1-OT.

3.2.1 Permeability of Hydraulic Fracture and Constant Pressure/Temperature Boundary Condition

The results of homogeneous and layered hydraulic fracture permeability as well as injection skin model and all surrounding boundary model (homogeneous permeability) are shown in Figure 15 and Figure 17. For the layered model, the center layer has permeability of 8e-10 m^2 and porosity of 0.2, one layer away from center layer has 2e-14 m^2 and 0.1, and then one layer further has 4.e-15 m^2 and 0.04, the farthest layer has 8e-16 m^2 and 0.01. Natural fractures have permeability of 1e-11 m^2 and porosity of 0.5.

Similar observations as the one-fracture model can be obtained here even the natural fractures exist in this system. When hydraulic fracture has a layered permeability, cold water tends to flow in the highly permeable layer and the matrix around injection point is not cooled down that fast (first and second row of Figure 17). The fracture temperature in the middle layer is reduced faster. When injection 'barrier' is set around the injection fracture, the pressure field of the whole system is changed ((f) in Figure 17). The injection pressure is shown in Figure 16 and the injection pressure is kept as high as 5300 psi. When 'all bound' is compared with 'homogeneous', it can be concluded that boundary condition seems not to have an impact as big as the one-fracture model. This is mainly because that thermal conduction from boundary layer is relatively farther from the hydraulic fracture. But it contributes a small portion to the production flow rate by

modifying the pressure field. The stable late stage flow rate out of E1-PB is around 330 ml/min, lower than 400 ml/min because of the production from the other wells. But still, this value does not match the desired ~100 ml/min.

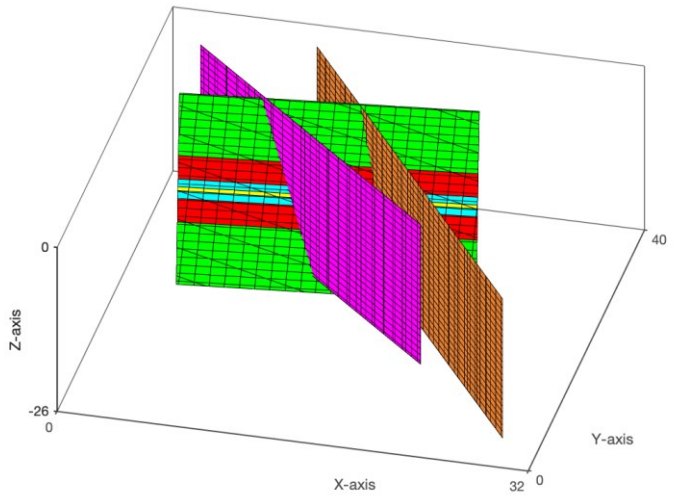

Figure 14 Embedded Discrete Fracture for three fracture model

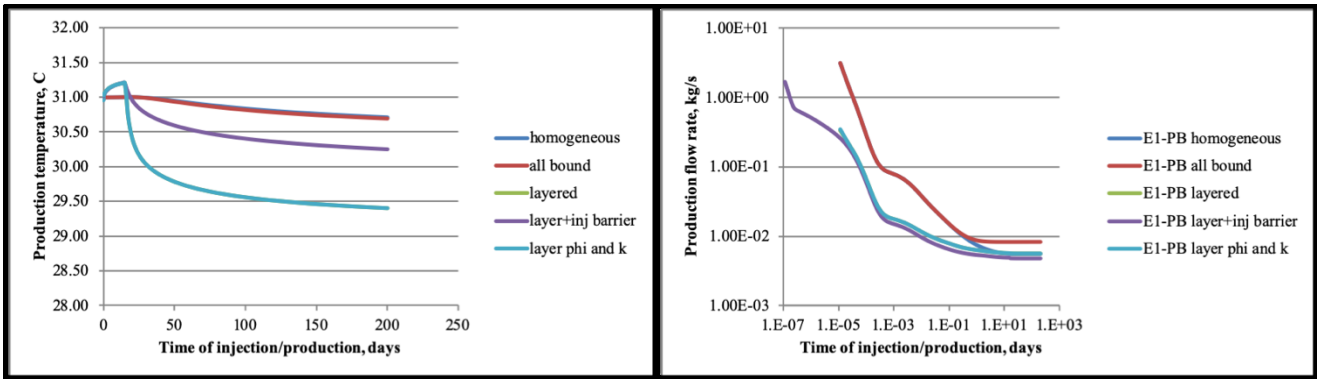

Figure 15 Production temperature and flow rate for (1) homogeneous hydraulic fracture permeability; (2) Constant pressure boundary; (3) Layered hydraulic fracture permeability; (4) Layered permeability + injection barrier around injection point; (5) Layered hydraulic fracture permeability and porosity

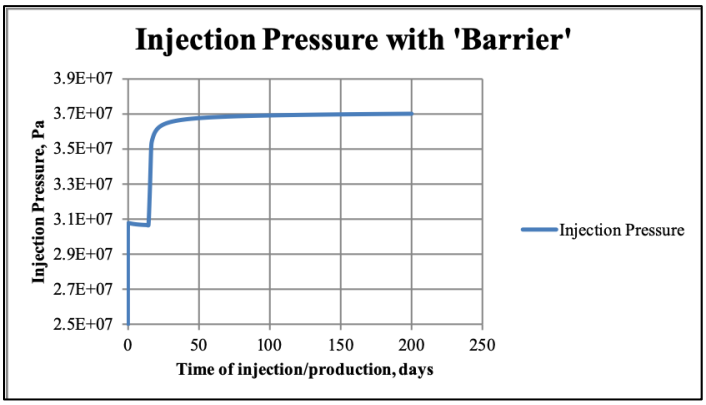

Figure 16 Injection pressure at injection well E1-I when injection skin (barrier) exists

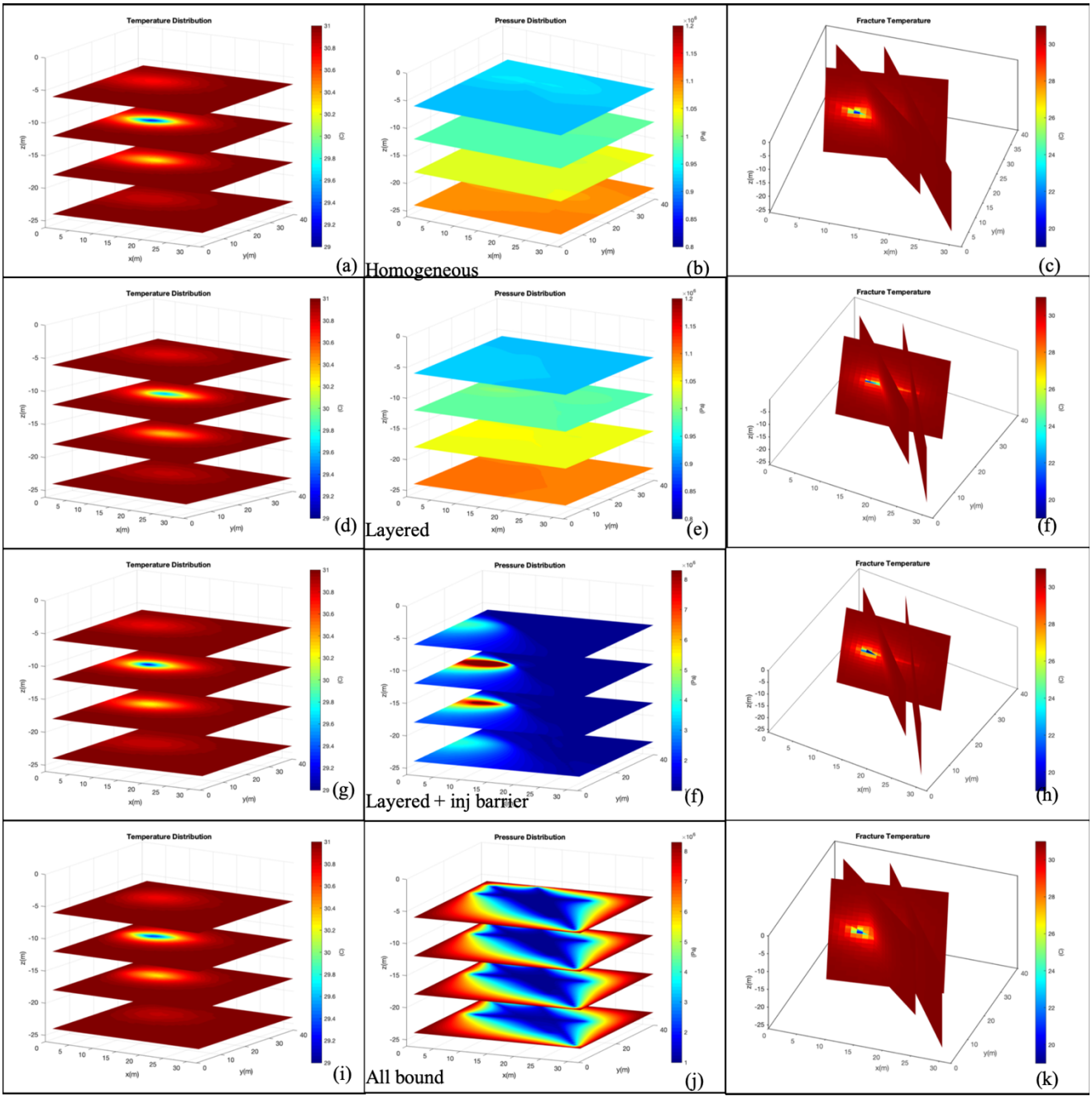

Figure 17 Temperature and pressure contour of matrix and temperature distribution in hydraulic fracture. The first, second, third and fourth row represent (1) homogeneous fracture permeability; (2) layered fracture permeability; (3) layered fracture permeability + inj barrier (4) constant pressure boundary. The first column is the matrix temperature, the second column is matrix pressure and third is fracture temperature.

3.2.2 Coupling Geomechanics with Three Fracture Model

Geomechanics does not affect the production temperature or flow rate much in the one fracture model. This effect will be evaluated again in this subsection. Geomechanics will be considered for homogeneous hydraulic fracture permeability and layered fracture permeability cases. Two natural fracture permeabilities are also varied (from 1e-11 to 8e-11 m^2) to check if permeability of natural fractures could affect the results. Production temperature, flow rate and pressure/temperature contour are shown in Figure 18 and Figure 19.

Comparing the red (layer) with dark blue line (layer+geomechanics), and light blue (homogeneous) with purple (homogeneous+geo+large NF) in Figure 18 gives us the implication that geomechanics does not have a big influence. Besides, the second comparison also implies that for homogeneous hydraulic fracture permeability, large natural fracture permeability does not slow down the cold-water penetration. However, the comparison between green and red indicates that for layer model, highly permeable natural fracture could bring hot water

into production well. Nevertheless, in terms of flow rate, geomechanics shrinks fracture permeability near the production side and large natural fracture system drains fluid to multiple production wells and hence flow out of EI-PB is slowed down to 140 ml/min, as shown in purple line Figure 18. This value is much closer to the measured data compared to other cases.

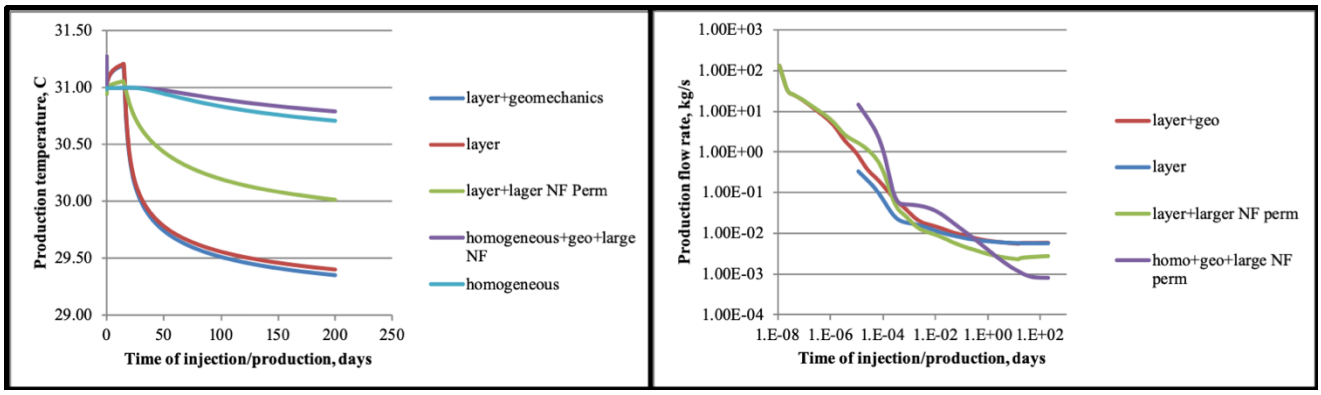

Figure 18 Production temperature and flow rate for three fracturing model comparing geomechanics

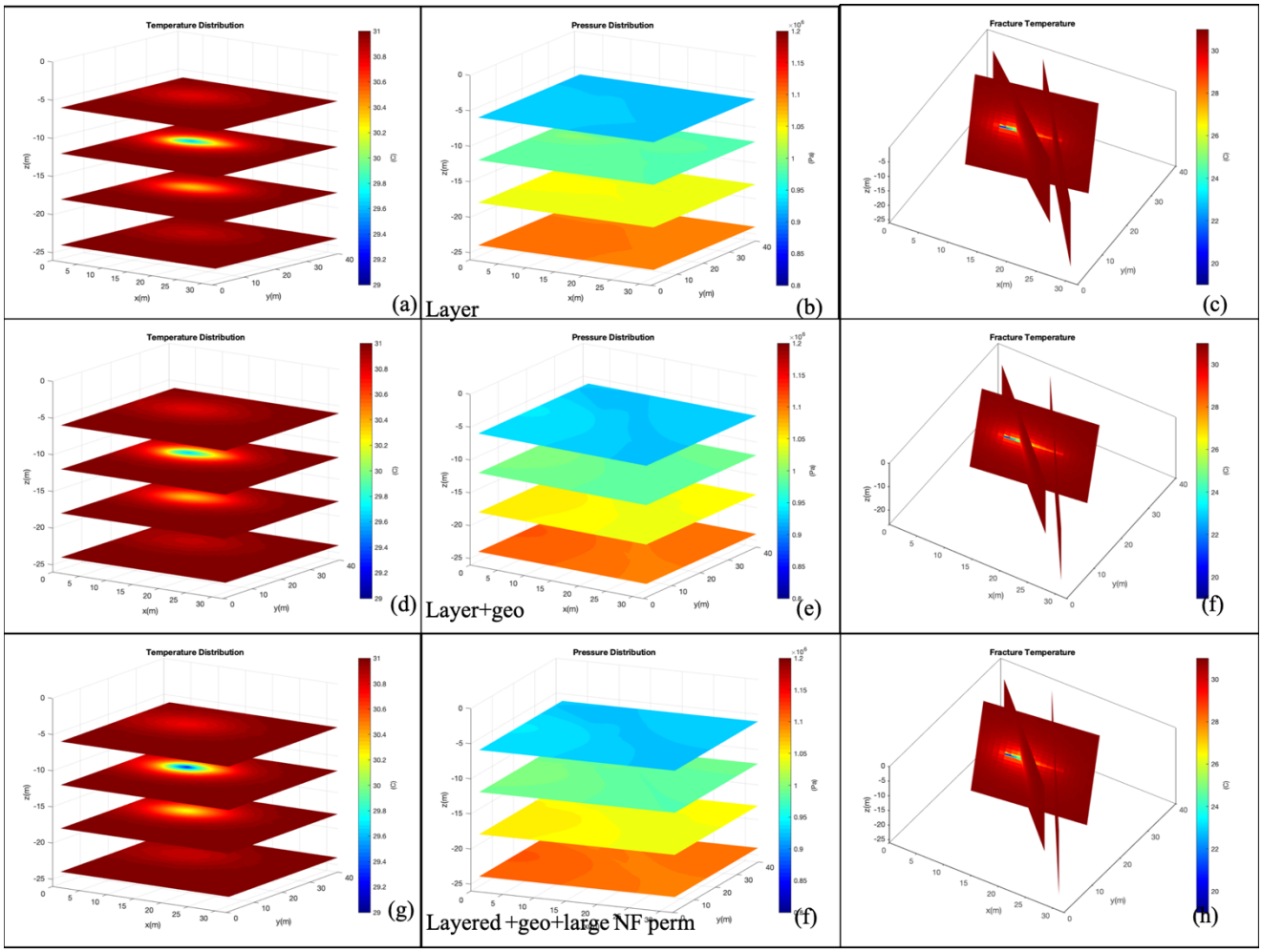

Figure 19 Temperature and pressure contour of matrix and temperature distribution in hydraulic fracture. The first, second, and third row represent (1) layered fracture permeability; (2) layered fracture permeability+geomechanics; (3) layered fracture permeability + geomechanics and large natural fracture permeability. The first column is the matrix temperature, the second column is matrix pressure and third is fracture temperature.

3.2.3 Temperature Gradient at EGS Collab Site and Fracture Tip Boundary

White et al. (2019) mentioned that actually the temperature is not constant all over the stimulation site. The closer to the tunnel, the cooler reservoir temperature can be expected. A rough estimation based on his study has been made and at two corner columns 32 °C and 24 °C are set to be constant temperature (and pressure) boundary. The initial temperature field is shown in Figure 20. When temperature gradient (from deep reservoir to tunnel) is considered, the starting temperature is different from previous case, which can be seen in Figure 21 (layer and layer+temp gradient). However, the temperature change has the same trend. Flow rates of these two situations are the same as well, which also proves that constant pressure boundary does not affect the fluid flow in fractures significantly. Even if the matrix blocks embedding fractures are set to be constant pressure boundary, due to the low permeability of matrix, not much difference is made. Based on the study of Beckers et al. (2020), the tracer test analysis indicates that there might be external fluid source supplementing the production. We designed a constant pressure boundary at one natural fracture grid on the low temperature side. As can be observed in Figure 21, the green and purple line shows that temperature production has been changed compared with the dark blue curve. Because of the constant cold water flow from the fracture tip, the temperature of both matrix and fracture drops down compared to the case without fracture tip boundary, as illustrated in Figure 22 ((a,d,g) and (c,f,h)). In addition to the temperature change, flow rate increases significantly as shown in Figure 21. This does not match the measurement very well.

We also compared the case with fracture tip boundary but without temperature gradient, which is shown in Figure 23. Obviously, hot water from fracture tip boundary is brought into hydraulic fracture to raise the production temperature, which is also reflected by the flat production curve (light blue) in Figure 21.

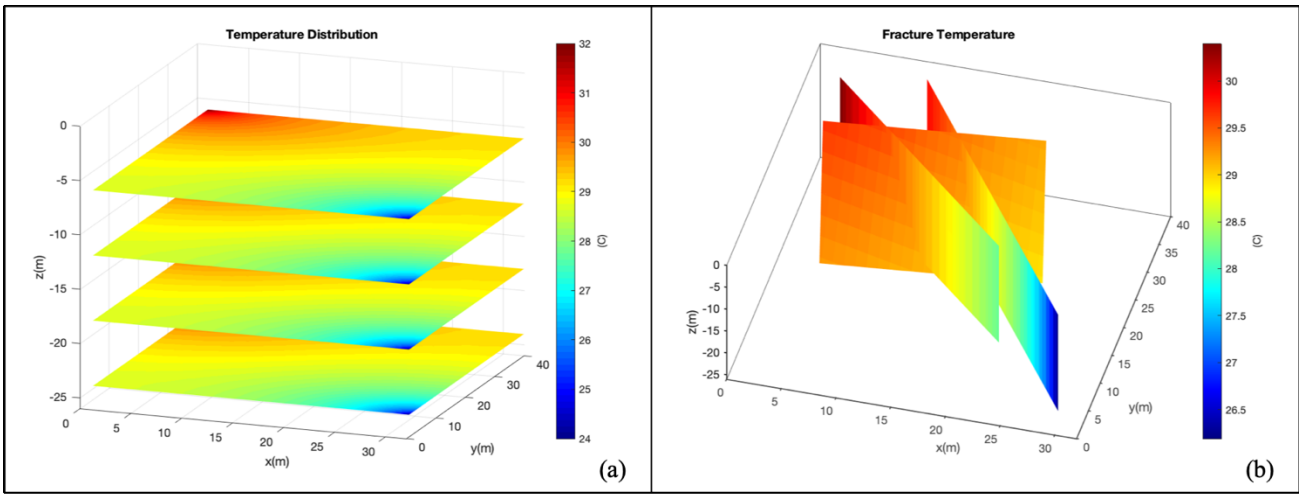

Figure 20 Initial temperature contour of matrix and fracture when temperature gradient is considered

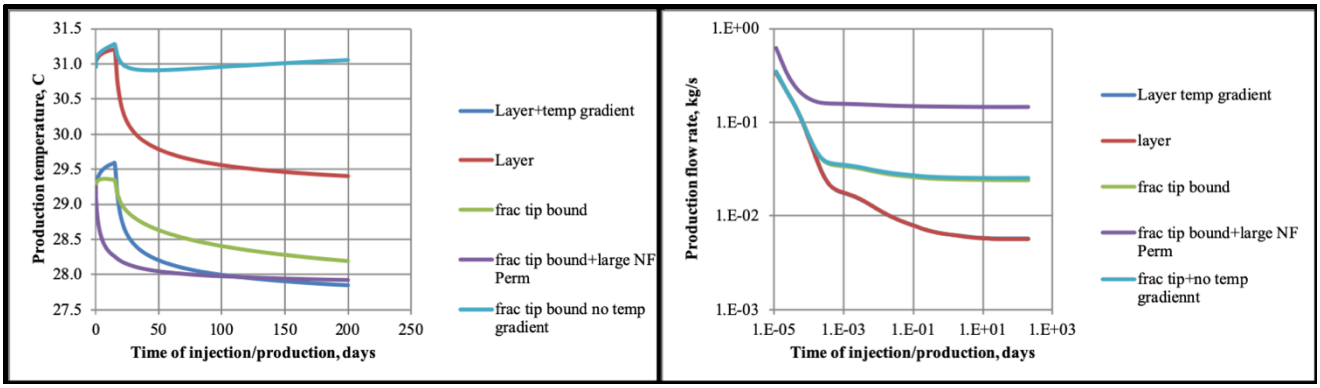

Figure 21 Production temperature and flow rate for (1) temperature gradient condition; (2) fracture tip boundary condition

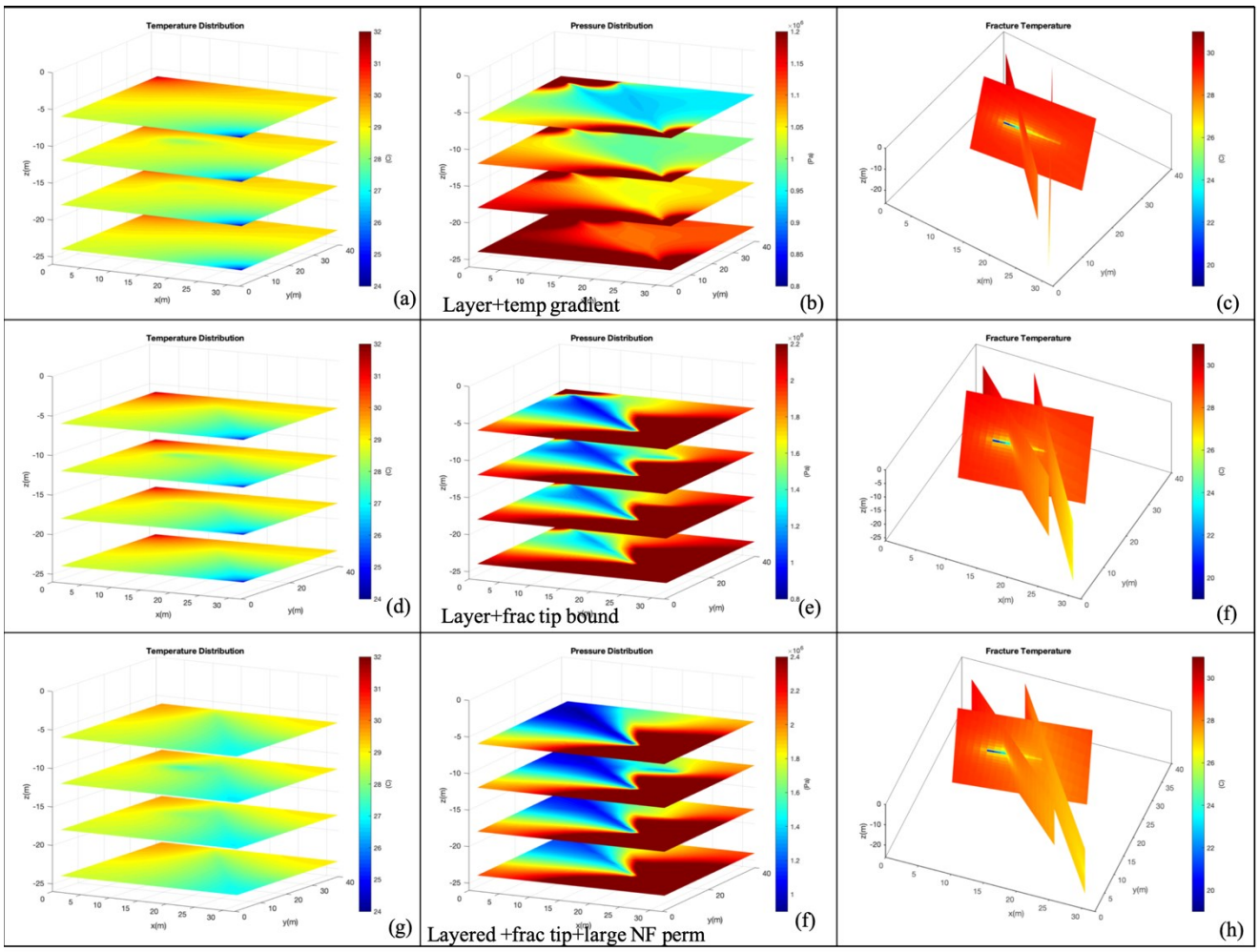

Figure 22 Temperature and pressure contour of matrix and temperature distribution in hydraulic fracture. The first, second, and third row represent (1) layered fracture permeability with temperature gradient across the reservoir; (2) layered fracture permeability+constant pressure and temperature boundary at fracture tip at the low temperature end; (3) layered fracture permeability + fracture tip boundary and large natural fracture permeability. The first column is the matrix temperature, the second column is matrix pressure and third is fracture temperature.

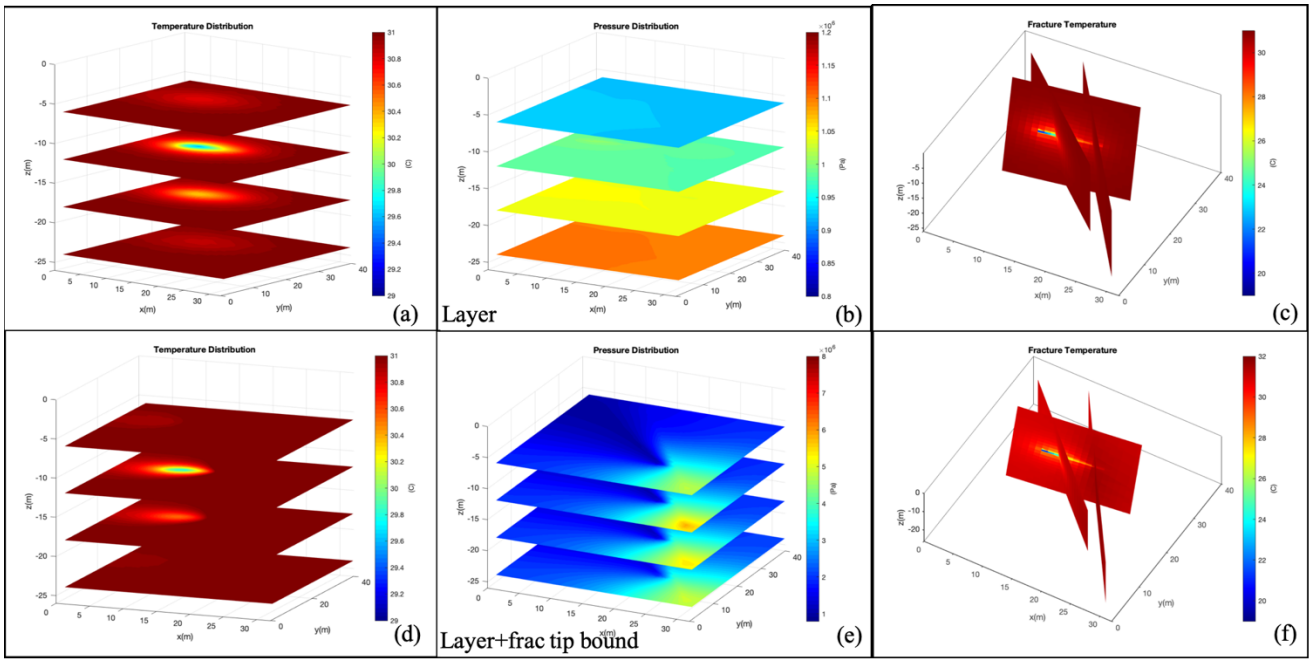

Figure 23 Temperature and pressure contour of matrix and temperature distribution in hydraulic fracture. The first and second row represent (1) layered fracture permeability base case; (2) layered fracture permeability+constant pressure and temperature boundary at fracture tip. The first column is the matrix temperature, the second column is matrix pressure and third is fracture temperature.

3.2.4 Potential Activated Natural Fracture System

Several studies proposed that a lot of natural fractures exist and may be activated during the stimulation process (Kneafsey et al., 2019; Neupane et al., 2019; Singh et al., 2019; White et al., 2019). In oil and gas industry, dense natural fractures can be conceptualized to a double porosity model. Inspired by this model, when the stimulation process is completed, a lot of natural factures can be activated and modeled using the mesh in Figure 24. Yellow fractures represent natural fracture systems. The permeability of natural fracture system is 4e-11 m^2.

The simulation results of this case, along with the base case, are plotted in Figure 25 and Figure 26. It can be seen that the existence of natural fractures weakens the temperature reduction when producing out of the well and the flow rate is also decreased because of flow within natural fracture system. Both of these results tend to match the field measurement. This indicates that it is highly likely that many natural fractures are activated and contribute to flow into fractures.

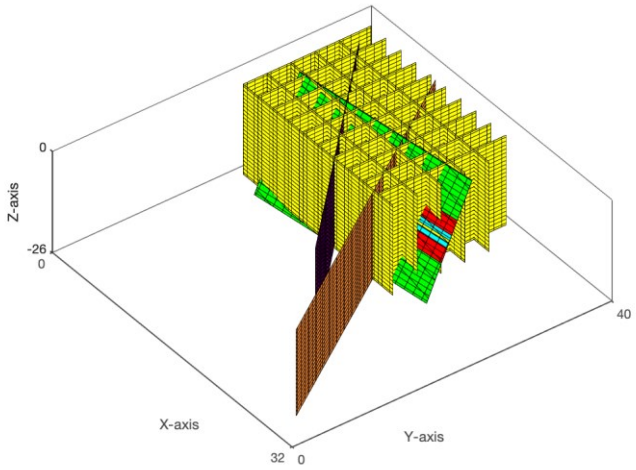

Figure 24 Schematic for three fracture model without activated natural fracture system

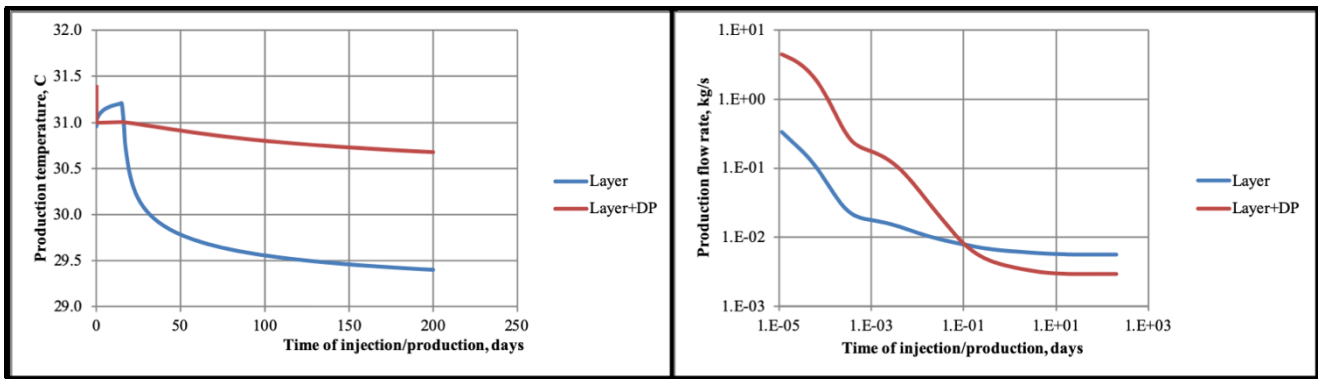

Figure 25 Production temperature and flow rate for comparison between with (Layer+DP) and without (Layer) natural fracture system.

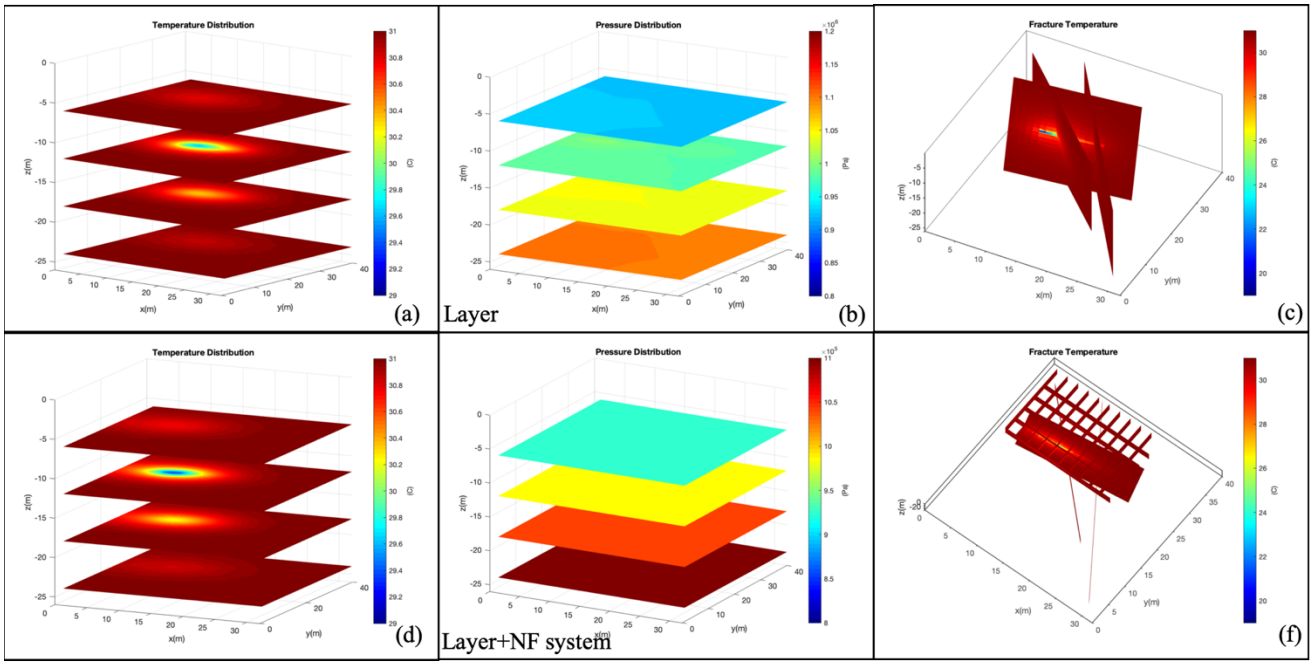

Figure 26 Temperature and pressure contour of matrix and temperature distribution in hydraulic fracture. The first and second row represent (1) without activated natural fracture system; (2) with activated natural fracture system. The first column is the matrix temperature, the second column is matrix pressure and third is fracture temperature.

3.2.5 Matching Production Flow Rate

In order to match the production flow rate, we have also tried another parameter input set for homogeneous hydraulic fracture permeability case. The input parameters are listed below in Table 3. Flow rate out of E1-PB, E1-PI are 80 ml/min and 198 ml/min, which match the measurement in Figure 3 very well. This also implies that it is possible to history match the flow rate by selecting permeability and PI sets. It also proves that the characterization of fracture system is very important for correct modeling input.

Table 3 Input parameter for matching flow rate

Parameter	Value	Unit
Hydraulic fracture permeability	8e-11	m^2
Shorter natural fracture permeability	1e-11	m^2
Longer natural fracture permeability	8e-10	m^2

PI of E1-PB	1e-11	m^2
PI of E1-PI	1e-10	m^2
PI of E1-PDT	1e-11	m^2
PI of E1-OT (@ longer natural fracture)	1e-12	m^2
PI of E1-OT (@ shorter natural fracture)	1e-12	m^2

4. DISCUSSION AND CONCLUSION

Based on the simulation results from various models and input parameters. It is obvious that permeability of fracture system, including hydraulic fracture and natural fractures, plays an important role in fluid and heat flow. Geomechanics will not affect production temperature but will impact flow rate out of the well. Boundary condition in large scale model might not be that important but should be contributing to the heat conduction to the fracture fluid, which means that in a small fracture model it does affect the production temperature. Activated natural fracture systems could be a potential reason why not much temperature change has been measured, and meanwhile they will impact the flow rate.

In this paper, we first introduce a developed model for coupled fluid/heat flow and geomechanics. And then the EDFM approach and its coupling with the THM model has been incorporated. Using these two models, we have performed a thorough reservoir simulation investigation on EGS Collab thermal circulation test at testbed 1, level 4,850. Main focuses of investigated modeling parameters include hydraulic fracture permeability, natural fracture permeability, geomechanics effect, boundary conditions, including matrix boundary and potential fracture tip boundary source, activated natural fracture system. The results show that these factors could impact the results of production temperature and flow rate to some extent. Aiming at matching the measured temperature and flow rate, permeability, natural fracture system, and geomechanics are among the most important variables. It has been shown in our simulation results that permeability can be modified to match the flow rate, activated natural fracture system could flatten the production temperature and geomechanics could lower down the flow rate. And meanwhile, if the skin effect is considered around the injection well, the observed high injection pressure is able to be explained as well. All of these results also prove the importance of measuring fracture aperture and permeability and characterizing fracture geometry. It is also desirable to use future temperature and flow rate data along with this coupled model to investigate the fractured reservoir and further improve the simulator as well. With more data collected, we can eliminate those assumptions that leads to an unmatched result and a relatively accurate model should be established at that time.

ACKNOWLEDGEMENT

The data used in this study was based on the measurement, monitoring of EGS Collab team. Some of the model set-ups originated or were borrowed from EGS Modeling and Simulation team teleconferences. The fracture model and input parameters resulted from the discussion with Koenraad Beckers and Bud Johnston. Thanks to their effort and suggestions, without which this study cannot be completed.

REFERENCES

Beckers, K., B. Johnston, N. Taverna, P. Winterfeld, and Y.-S. Wu, 2020, Analysis of EGS-Collab Tracer and Thermal Tests using Analytical and Numerical Tools: In progress.

Chai, C., M. Maceira, and H. Santos Villalobos, 2019, Subsurface Seismic Structure Around the Sanford Underground Research Facility, *in* 44th Workshop on Geothermal Reservoir Engineering.

Chen, Y., L. Huang, M. Schoenball, J. Ajo-Franklin, T. J. Kneafsey, and E. C. Team, 2019, Real-Time Microearthquake Event Detection and Location Using a Multiscale Scanning Approach for EGS Collab Experiments, *in* 44th Workshop on Geothermal Reservoir Engineering.

Frash, L. P., J. W. Carey, N. J. Welch, and E. C. Team, 2019, EGS Collab Experiment 1 Geomechanical and Hydrological Properties by Triaxial Direct Shear Multiple affiliations; team members listed in acknowledgements, *in* 44th Workshop on Geothermal Reservoir Engineering.

Fu, P., M. Schoenball, J. Morris, J. Ajo-Franklin, H. Knox, T. Kneafsey, J. Burghardt, and M. White, 2019, Microseismic Signatures of Hydraulic Fracturing: A Preliminary Interpretation of Intermediate-Scale Data from the EGS Collab Experiment 1, *in* 44th Workshop on Geothermal Reservoir Engineering.

Gutierrez, M., R. W. Lewis, and I. Masters, 2001, Petroleum Reservoir Simulation Coupling Fluid Flow and Geomechanics: SPE Reservoir Evaluation & Engineering, v. 4, no. 03, p. 164–172, doi:10.2118/72095-PA.

Hu, L., P. H. Winterfeld, P. Fakcharoenphol, and Y.-S. Wu, 2013, A novel fully-coupled flow and geomechanics model in enhanced geothermal reservoirs: Journal of Petroleum Science and Engineering, v. 107, p. 1–11, doi:10.1016/J.PETROL.2013.04.005.

Kim, J., and G. J. Moridis, 2013, Development of the T+M coupled flow–geomechanical simulator to describe fracture propagation and coupled flow–thermal–geomechanical processes in tight/shale gas systems: Computers & Geosciences, v. 60, p. 184–198, doi:10.1016/J.CAGEO.2013.04.023.

Kim, J., H. A. Tchelepi, and R. Juanes, 2009, Stability, Accuracy and Efficiency of Sequential Methods for Coupled Flow and Geomechanics, *in* SPE Reservoir Simulation Symposium: Society of Petroleum Engineers, doi:10.2118/119084-MS.

Kneafsey, T. J. et al., 2019, EGS Collab Project: Status and Progress, *in* 44th Workshop on Geothermal Reservoir Engineering.

Lee, S. H., M. F. Lough, and C. L. Jensen, 2001, Hierarchical modeling of flow in naturally fractured formations with multiple length scales: Water Resources Research, v. 37, no. 3, p. 443–455, doi:10.1029/2000WR900340.

Lu, J., and A. Ghassemi, 2019, Coupled Thermo-Hydro-Mechanical-Seismic Modeling of Fractured Reservoir Stimulation with Application to EGS Collab, *in* 44th Workshop on Geothermal Reservoir Engineering.

Mattson, E. D., Y. Zhang, A. Hawkins, T. Johnson, J. Ajo-Franklin, G. H. Neupane, and M. A. Plummer, 2019, Preliminary Collab Fracture Characterization Results from Flow and Tracer Testing Efforts, *in* 44th Workshop on Geothermal Reservoir Engineering: doi:10.15121/1593283.

McDermott, C., and O. Kolditz, 2006, Geomechanical model for fracture deformation under hydraulic, mechanical and thermal loads: Hydrogeology Journal, v. 14, no. 4, p. 485–498, doi:10.1007/s10040-005-0455-4.

Min, K.-B., J. Rutqvist, C.-F. Tsang, and L. Jing, 2004, Stress-dependent permeability of fractured rock masses: a numerical study: International Journal of Rock Mechanics and Mining Sciences, v. 41, no. 7, p. 1191–1210, doi:10.1016/J.IJRMMS.2004.05.005.

Moinfar, Ali, 2013, Development of an efficient embedded discrete fracture model for 3D compositional reservoir simulation in fractured reservoirs.

Moinfar, A., A. Varavei, K. Sepehrnoori, and R. T. Johns, 2012, Development of a Novel and Computationally-Efficient Discrete-Fracture Model to Study IOR Processes in Naturally Fractured Reservoirs, *in* SPE Improved Oil Recovery Symposium: Society of Petroleum Engineers, doi:10.2118/154246-MS.

Neupane, G., R. Podgorney, H. Huang, and E. Mattson, 2019, EGS Collab Earth Modeling: Integrated 3D Model of the Testbed: GRC Transactions, v. 43.

Oldenburg, C. M. et al., 2016, Intermediate-Scale Hydraulic Fracturing in a Deep Mine kISMET Project Summary 2016.

Rutqvist, J., 2011, Status of the TOUGH-FLAC simulator and recent applications related to coupled fluid flow and crustal deformations: Computers & Geosciences, v. 37, no. 6, p. 739–750, doi:10.1016/J.CAGEO.2010.08.006.

Rutqvist, J., Y.-S. Wu, C.-F. Tsang, and G. Bodvarsson, 2002, A modeling approach for analysis of coupled multiphase fluid flow, heat transfer, and deformation in fractured porous rock: International Journal of Rock Mechanics and Mining Sciences, v. 39, no. 4, p. 429–442, doi:10.1016/S1365-1609(02)00022-9.

Schoenball, M. et al., 2019, Microseismic monitoring of meso-scale stimulations for the DOE EGS Collab project at the Sanford Underground Research Facility, *in* 44th Workshop on Geothermal Reservoir Engineering.

Settari, A., and D. A. Walters, 2001, Advances in Coupled Geomechanical and Reservoir Modeling With Applications to Reservoir Compaction: SPE Journal, v. 6, no. 03, p. 334–342, doi:10.2118/74142-PA.

Singh, A., G. Neupane, P. Dobson, M. Zoback, and J. Morris, 2019, Slip Tendency Analysis of Fracture Networks to Determine Suitability of Candidate Testbeds for the EGS Collab Hydroshear Experiment: GRC Transactions, v. 43.

Tran, D., A. Settari, and L. Nghiem, 2004, New Iterative Coupling Between a Reservoir Simulator and a Geomechanics Module: SPE Journal, v. 9, no. 03, p. 362–369, doi:10.2118/88989-PA.

Wang, C., 2018, A multi-scale, multi-continuum and multi-physics model to simulate coupled fluid flow and geomechanics in shale gas reservoirs.

Wang, S., Z. Huang, Y.-S. Wu, P. H. Winterfeld, and L. E. Zerpa, 2016, A semi-analytical correlation of thermal-hydraulic-mechanical behavior of fractures and its application to modeling reservoir scale cold water injection problems in enhanced geothermal reservoirs: Geothermics, v. 64, p. 81–95, doi:10.1016/J.GEOTHERMICS.2016.04.005.

Wang, C., Q. Ran, and Y. S. Wu, 2019, Robust implementations of the 3D-EDFM algorithm for reservoir simulation with complicated hydraulic fractures: Journal of Petroleum Science and Engineering, v. 181, doi:10.1016/j.petrol.2019.106229.

White, M. et al., 2019, The Necessity for Iteration in the Application of Numerical Simulation to EGS: Examples from the EGS Collab Test Bed 1, *in* 44th Workshop on Geothermal Reservoir Engineering.

Winterfeld, P. H., and Y.-S. Wu, 2012, A Novel Fully Coupled Geomechanical Model for CO2 Sequestration in Fractured and Porous Brine Aquifers, *in* XIX International Conference on Water Resources.

Winterfeld, P. H., and Y.-S. Wu, 2016, Simulation of Coupled Thermal/Hydrological/Mechanical Phenomena in Porous Media: SPE Journal, v. 21, no. 03, p. 1041–1049, doi:10.2118/173210-PA.

Wu, H., P. Fu, J. P. Morris, E. D. Mattson, A. J. Hawkins, Y. Zhang, R. R. Settgast, F. J. Ryerson, and E. C. Team, 2019, Characterizing Fracture Flow in EGS Collab Experiment Based on Stochastic Modeling of Tracer Recovery, *in* 44th Workshop on Geothermal Reservoir Engineering.

Wu, Y. S., K. Zhang, C. Ding, K. Pruess, E. Elmroth, and G. S. Bodvarsson, 2002, An efficient parallel-computing method for modeling nonisothermal multiphase flow and multicomponent transport in porous and fractured media: Advances in Water Resources, v. 25, no. 3, p. 243–261, doi:10.1016/S0309-1708(02)00006-4.

Xu, Y., J. S. A. Cavalcante Filho, W. Yu, and K. Sepehrnoori, 2017, Discrete-Fracture Modeling of Complex Hydraulic-Fracture Geometries in Reservoir Simulators: SPE Reservoir Evaluation & Engineering, v. 20, no. 02, p. 403–422, doi:10.2118/183647-PA.

Yu, X., P. Winterfeld, S. Wang, C. Wang, L. Wang, and Y. Wu, 2019, A Geomechanics-Coupled Embedded Discrete Fracture Model and its Application in Geothermal Reservoir Simulation, *in* SPE Reservoir Simulation Conference: Society of Petroleum Engineers, doi:10.2118/193931-MS.

Zhang, K., Y. S. Wu, C. Ding, K. Pruess, and E. Elmroth, 2001, Parallel Computing Techniques for Large-Scale Reservoir Simulation of Multi-Component and Multiphase Fluid Flow, *in* SPE Reservoir Simulation Symposium: Society of Petroleum Engineers, doi:10.2118/66343-MS.